

The Magnitude-Size Relation of Galaxies out to $z \sim 1$ ^{1,2}

Luc Simard³, David C. Koo, S. M. Faber, Vicki L. Sarajedini, Nicole P. Vogt^{3,4}, Andrew C. Phillips, Karl Gebhardt, Garth D. Illingworth, K. L. Wu
UCO/Lick Observatory, University of California, Santa Cruz, CA 95064, USA

ABSTRACT

As part of the Deep Extragalactic Evolutionary Probe (DEEP) survey, a sample of 190 field galaxies ($I_{814} \leq 23.5$) in the “Groth Survey Strip” has been used to analyze the magnitude-size relation over the range $0.1 < z < 1.1$. The survey is statistically complete to this magnitude limit. All galaxies have photometric structural parameters, including bulge fractions (B/T), from Hubble Space Telescope images, and spectroscopic redshifts from the Keck Telescope. The analysis includes a determination of the survey selection function in the magnitude-size plane as a function of redshift, which mainly drops faint galaxies at large distances. Our results suggest that selection effects play a very important role.

A first analysis treats disk-dominated galaxies with $B/T < 0.5$. If selection effects are ignored, the mean disk surface brightness (averaged over all galaxies) increases by ~ 1.3 mag from $z = 0.1$ to 0.9 . However, most of this change is plausibly due to comparing low luminosity galaxies in nearby redshift bins to high luminosity galaxies in distant bins. If this effect is allowed for, no discernible evolution remains in the disk surface brightness of bright ($M_B < -19$) disk-dominated galaxies. A second analysis treats all galaxies by substituting half-light radius for disk scale length, with similar conclusions. Indeed, at all redshifts, the bulk of galaxies is consistent with the magnitude-size envelope of local galaxies, i.e., with little or no evolution in surface brightness. In the two highest redshift bins ($z > 0.7$), a handful of luminous, high surface brightness galaxies appears that occupies a region of the magnitude-size plane rarely populated by local galaxies. Their wide range of colors and bulge fractions points to a variety of possible origins.

Subject headings: galaxies:fundamental parameters, galaxies:evolution

¹Based on data obtained at the W.M. Keck Observatory, which is operated as a scientific partnership among the California Institute of Technology, the University of California and the National Aeronautics and Space Administration. The Observatory was made possible by the generous financial support of the W.M. Keck Foundation.

²Based on observations made with the NASA/ESA *Hubble Space Telescope* which is operated by AURA, Inc., under contract with NASA.

³Guest User, Canadian Astronomy Data Center, which is operated by the National Research Council of Canada, Herzberg Institute of Astrophysics, Dominion Astrophysical Observatory

⁴Current Address: Institute of Astronomy, University of Cambridge, Cambridge CB3 0HE, England, UK

1. Introduction

The field of galaxy evolution is rapidly changing under the wealth of new data coming from powerful instruments such as the Hubble Space Telescope (*HST*) and 10-m class telescopes. Given the complexity of the problem, any attempt at understanding galaxy evolution must be deeply rooted in a quantitative and systematic study of fundamental galaxy structural parameters such as luminosity, size, mass *and* their associated scaling relations. High-redshift galaxies were first studied through their global luminosity function. The landmark Canada-France Redshift Survey (CFRS, Lilly et al. 1995) showed that the luminosity function of blue galaxies evolves significantly over the redshift range $0.0 < z < 1.0$ while that of red galaxies shows little or no evolution over the same redshift range. However, luminosity functions cannot paint a complete picture of the evolution of galaxies, as luminosity is only one of many galaxy structural parameters that may be evolving.

Since individual galaxies cannot be observed at different epochs, galaxy evolution can be operationally defined as the statistical change in galaxy properties with redshift. Correlations between observables such as total absolute magnitude M , half-light radius R_{hl} , disk scale length R_d , and rotation speed V_c are particularly powerful diagnostics, as they involve key global properties of galaxies, namely luminosity, size, and mass. Furthermore, shifts in the zeropoints of such correlations are fairly insensitive to the local densities of objects, and co-moving volume densities are therefore not required.

So far, two galaxy scaling relations have been explored at moderate redshifts. The $M - V_c$ relation, also more commonly known as the Tully-Fisher (TF) relation, has been studied to $z \sim 1$ by Vogt et al. (1996,1997). Based on only 16 galaxies, they found that: (1) massive, mature disks were present at $z \sim 1$, and (2) the change in the TF B-band zeropoint of these disks was at most 0.4 mag. Using ground-based CCD images, Schade et al. (1996a,b) presented $R_d - M_{disk}$ relations over the redshift range $0.1 < z < 0.6$ for 351 late-type field and cluster galaxies and $R_e - M_{bulge}$ relations for 166 early-type field and cluster galaxies over the same redshift range. Both samples were taken from the ground-based Canadian Network for Observational Cosmology (CNOC) sample. The late-type galaxy magnitude-size relations showed an apparent increase in disk surface bright-

ness of ~ 1 mag at a given R_d by $z = 0.6$, both in the outer regions of clusters and in the field. Similarly, the effective surface brightness of early-type galaxies seemed to increase by 0.7 mag at $z = 0.6$. Using *HST* data, Roche et al. (1998) studied the surface brightness and size of 270 galaxies out to $z = 4$ taken from various redshift surveys. They found that the mean rest-frame blue-band surface brightness at a fixed radius seemed to increase smoothly by 0.95 mag between $z = 0.2$ and $z = 0.9$. They also concluded that a Pure Luminosity Evolution (PLE) model was not sufficient to explain the observed evolution in surface brightness and proposed a Size-Luminosity Evolution (SLE) model based on the evolution of different stellar populations as a function of galactocentric distance. Lilly et al. (1998) concluded from *HST* structural parameters of 341 CFRS and LDSS galaxies that the increase in the disk surface brightness with redshift for galaxies with disk scale lengths greater than $4 h_{50}^{-1}$ kpc was 0.8 ± 0.3 mag. This increase was not sufficient to account for the evolution of the overall luminosity function of galaxies seen in the CFRS survey over the interval $0 < z < 1$. They suggested that smaller galaxies were responsible for most of the observed evolution, but they could not conclusively verify that hypothesis due to their magnitude and radius limits.

The question of whether the apparent evolution seen in galaxies at high redshifts is operating in both luminosity and/or size has received considerable attention in a recent flurry of theoretical activity aimed at explaining the formation and evolution of disk galaxies (Bouwens, Cayón & Silk 1997; Dalcanton, Spergel & Summers 1997; Mo, Mao & White 1997; Mao, Mo & White 1998; Contardo, Steinmetz & Fritze-von Alvensleben 1998; Firmani & Avila-Reese 1998). Certain semi-analytical no-infall models (e.g., Mo, Mao & White 1997) predict that disk scale length should vary as $(1+z)^{-1}$ in an $\Omega = 1$ universe. Smaller disk scale lengths would be expected in the past due to the increase in the critical density ρ_{crit} of the Universe with look-back time. Dark matter halos are defined with a fixed overdensity ($\rho_{mean}^{halo} \sim 200\rho_{crit}$) in numerical simulations, and the radius of those halos must therefore decrease with increasing redshift to meet the overdensity criterion at high redshifts. Assuming that the mass and angular momentum of the gas settling into disks are fixed fractions of the mass and angular momentum of dark matter halos, smaller halo radii will translate into smaller disk scale

lengths. Infall models (e.g., Chiappini, Matteucci & Gratton 1997), on which the SLE model of Roche et al. (1998) is based, predict a milder disk size evolution. Disk sizes at $z \sim 1$ in these models are typically only 20% smaller than at $z = 0$. Disk size is therefore important by itself to distinguish between these different scenarios even though, as pointed out by Mao, Mo, & White (1998), it is likely that only kinematic information can decisively separate evolution in the mass and size of galaxies from evolution in their stellar mass-to-light ratio.

One of the goals of the Deep Extragalactic Evolutionary Probe (DEEP; Koo 1998) survey is to compare the full 3D distribution of galaxy size, luminosity and rotation velocity at high redshift to local relations (e.g., Burstein et al. 1997; hereafter BBFN) using a deep, homogenous sample of galaxies observed with the Hubble Space Telescope (*HST*) and the 10-m W.M. Keck Telescope. As a first step towards this goal, this paper focuses on the galaxy magnitude-size relation and seeks to extend previous work to fainter disk luminosities and higher redshifts. A major new focus is the role of selection effects. As this paper will show, selection effects have had a major impact on the conclusions drawn from previous studies of the magnitude-size relation. Further photometric data, internal velocities and full 3D structural distributions on larger samples of DEEP galaxies will follow in future papers.

Section 2 describes the sample and observational measurements of galaxy sizes and magnitudes. Selection effects are quantified in Section 2.3. The magnitude-size relation as a function of redshift is presented in Section 3, and its implications for galaxy evolution are discussed in Section 4. Values of $H_0 = 70 \text{ km s}^{-1} \text{ Mpc}^{-1}$ and $q_0 = 0.1$ are used throughout this paper so that L^* galaxies have $I \sim 22.9$ at $z \sim 1$ with $1''$ corresponding to 7.3 kpc. It should be noted that surface brightness is independent of q_0 . All magnitudes are on the Vega-based system ($I_{814, \text{Vega}} = I_{814, \text{AB}} - 0.44$).

2. Observations and Analysis

2.1. HST Structural Measurements

The *HST* data are from two surveys, which we dub the ‘‘Groth Survey Strip’’ (GSS), taken under *HST* programs GTO 5090 and GTO 5109. The GSS consists of 28 overlapping subfields taken with the *HST* Wide Field and Planetary Camera (WFPC2)

and forms a ‘‘chevron strip’’ oriented NE to SW at roughly 1417+52 at Galactic latitude $b \sim 60^\circ$. Each of 27 subfields has exposures of 2800 s in the broad *V* filter (*F606W*) and 4400 s in the broad *I* filter (*F814W*). The 28th field is the Deep Field (J2000 1417.5+52.5), with total exposures of 24,400 s in *V* and 25,200 s in *I*. The images were recalibrated ‘‘on-the-fly’’ through the Canadian Astronomy Data Center (CADC) standard pipeline and coadded with the IRAF⁵/STSDAS task CRREJ to remove cosmic rays.

Object catalogs were produced with SExtractor version 1.0a (Bertin & Arnouts 1996) using a detection threshold of 1.5σ and a minimum detection area of 10 contiguous pixels. SExtractor also produced a ‘‘segmentation’’ or ‘‘mask’’ image which was used to deblend galaxies from their nearby companions. Pixels belonging to the same object are all assigned the same flag in this segmentation image, so the SExtractor segmentation image was ideal for isolating objects in the surface brightness profile fits.

The surface brightness profiles of galaxies in the DEEP/GSS sample were fitted with a PSF-convolved 2D bulge+disk model (GIM2D: Simard 1998, Marleau & Simard 1998). The model had a *maximum* of twelve parameters: the flux F_{total} in data units (DU) integrated out to $r = \infty$, the bulge fraction B/T ($\equiv F_{bulge}/F_{total}$), the bulge effective radius r_e , the bulge ellipticity e ($e \equiv 1 - b/a$, $b \equiv$ semi-minor axis, $a \equiv$ semi-major axis), the bulge position angle of the major axis ϕ_b , the exponential disk scale length r_d , the disk inclination i (face-on $\equiv 0$), the disk position angle ϕ_d , the subpixel dx and dy offsets of the galaxy center, the background level b , and the Sérsic index n .

The first component (the ‘‘bulge’’) of the 2D surface brightness model was a Sérsic profile of the form:

$$\Sigma(r) = \Sigma_e \exp\{-k[(r/r_e)^{1/n} - 1]\} \quad (1)$$

where $\Sigma(r)$ is the surface brightness at r along the semi-major axis in linear flux units per unit area, and Σ_e is the effective surface brightness. The parameter k was set equal to $1.9992n - 0.3271$ so that r_e remained the projected radius enclosing half of the light in this component. The classical de Vaucouleurs profile has the special value $n = 4$, and this value was

⁵IRAF is distributed by the National Optical Astronomy Observatories, which are operated by the Association of Universities for Research in Astronomy, Inc., under cooperative agreement with the National Science Foundation.

chosen for the current analysis. This choice was motivated by studies of bulge profiles in local galaxies. Locally, there is evidence that the bulges of late-type spiral galaxies may be better fitted by an $n = 1$ profile, whereas bright ellipticals and the bulges of early-type spiral galaxies follow an $n = 4$ profile (de Jong 1994, Courteau et al. 1996, Andredakis 1998). Local late-type galaxies with $n = 1$ bulges have $B/T \leq 0.1$ (de Jong 1994). Since such bulges contain only 10% of the total galaxy light, low signal-to-noise measurements of late-type high-redshift galaxies make it very difficult to determine the Sérsic index. On the other hand, n is more important for bulge-dominated galaxies, and $n = 4$ is the expected value based on early-type local galaxies. The total flux in the Sérsic bulge component is calculated by integrating Equation 1 from $r = 0$ to infinity to obtain:

$$F_{bulge} = 2\pi n e^k k^{-2n} r_e^2 \Gamma(2n) \Sigma_e \quad (2)$$

where Γ is the incomplete gamma function. For $n = 4$, $F_{bulge} = 7.214\pi r_e^2 \Sigma_e$.

The second component (the “disk”) was a simple exponential profile of the form:

$$\Sigma(r) = \Sigma_0 \exp(-r/r_d), \quad (3)$$

where Σ_0 is the central surface brightness. The total flux in the disk is given by:

$$F_{disk} = 2\pi r_d^2 \Sigma_0. \quad (4)$$

A PSF-deconvolved half-light radius r_{hl} was also computed for each galaxy by integrating the sum of Equations 1 and 3 out to infinity with the best fitting structural parameters. Even though the conventional “bulge/disk” nomenclature has been adopted in this paper, it should be kept in mind that this nomenclature does not say anything about the internal kinematics of the components. The presence of a “disk” component does not necessarily imply the presence of an actual disk since many dynamically hot systems also have simple exponential profiles of the form given by Equation 3 (Lin & Faber 1983, Kormendy 1985). Likewise a “bulge” may represent a brightened center due to a starburst rather than a genuine dynamically hot spheroid.

WFPC2 detector undersampling was taken into account by generating the surface brightness model on an oversampled grid, convolving it with the appropriate point spread function (PSF), shifting its cen-

ter according to dx and dy , and rebinning the result to the detector resolution for direct comparison with the observed galaxy image. The PSF was generated by the Space Telescope package *TINY TIM* (Krist 1993) and subsampled to reproduce the pixel resolution of the Wide-Field camera. The best fitting parameter values were found with the Metropolis Algorithm (Metropolis et al. 1953, Saha & Williams 1994), which Monte-Carlo samples parameter space to maximize the likelihood function. Best parameter values and their confidence intervals were determined simultaneously by the algorithm as it refined its best solution. Figure 1 shows a $55'' \times 45''$ section of a typical WFPC2/F814W GSS image before and after GIM2D processing. Figure 2 shows examples of GIM2D surface brightness fits for a set of five galaxies covering a wide range of bulge fractions and redshifts.

Following the simulation procedure described in Section 3.4 of Marleau & Simard (1998), 400 simulated GSS galaxies were created with a wide range of structural parameters and analyzed in exactly the same way as real galaxies to test the reliability of the GSS parameter values measured with GIM2D. For simulated disk-dominated galaxies ($B/T \leq 0.5$) brighter than $I_{814} = 23.5$, the mean difference between the measured and input disk magnitudes $\langle \Delta I_{814}(disk) \rangle$ was -0.02 with $\sigma(\Delta I_{814}(disk)) = 0.20$. For the same galaxies, the mean difference between the measured and input log disk scale lengths $\langle \Delta \log r_d \rangle$ was 0.02 , and $\sigma(\Delta \log r_d)$ was 0.05 . Errors in bulge+disk fits are discussed in greater details in Marleau & Simard (1998).

2.2. Keck/LRIS Spectroscopy

GSS galaxies are currently being systematically surveyed by the DEEP team using the multi-object Low Resolution Imaging Spectrograph (LRIS, Oke et al. 1995) on the W.M. Keck II Telescope. DEEP/GSS galaxies were selected according to the magnitude criterion $(V + I)/2 < 24$. Spectra of a first group of 231 galaxies were acquired between May 1995 and May 1997, and these are the galaxies used in this paper. Two gratings were used to cover a total spectral range of about 4500–9100 Å depending on the exact position of the target on the mask: a 900 lines mm^{-1} grating (central wavelength $\simeq 5800$ Å, dispersion = 0.85 Å/pixel and resolution ~ 3 – 4 Å FWHM), and a 600 lines mm^{-1} grating (central wavelength $\simeq 7700$ Å, dispersion = 1.26 Å/pixel and resolution ~ 4 – 5 Å FWHM). Typical total exposure time

per target and per grating was 2700 seconds. Rectified, wavelength-calibrated, sky-subtracted 2D spectra were produced with a custom LRIS reduction package. One-dimensional spectra were optimally extracted using the IRAF/APEXTRACT package. Details of the spectral data reduction will be given elsewhere. The final DEEP/GSS sample has a total of 217 objects with both Keck redshifts and *HST* structural parameters. The sample was cut down further to 190 galaxies by selecting only galaxies brighter than $I_{814} = 23.5$. The DEEP/GSS redshift sample is 100% statistically complete down to $I_{814} = 23.5$, meaning that redshifts were obtained for every object targeted spectroscopically above that limit. However, the redshift sample is not spatially complete since not all objects brighter than $I_{814} = 23.5$ were targeted. Furthermore, the basic photometric catalog may not be complete to $I_{814} = 23.5$ if low surface brightness galaxies are lost in the SExtractor selection process. This effect is discussed below but does not appear to affect our major conclusions.

2.3. Selection Effects

Since selection effects can conceivably mimic real evolutionary changes in the high-redshift galaxy population, it is important to determine how they affect the DEEP/GSS sample. This section describes selection effects both qualitatively and quantitatively.

2.3.1. Observed Structural Parameter Distributions

In order to determine whether the sample of galaxies with redshifts is an unbiased representation of the photometric catalog population in the GSS, the observed structural parameter distributions of galaxies with Keck redshifts were first compared to those of 725 general field galaxies measured in the same 6 fields of the GSS covered by the spectroscopic sample so far. These galaxies were photometrically selected using SExtractor and then cut at $I_{814} = 23.5$, just like the sample of redshift galaxies. They should therefore be an equivalent sample, differing only in their lack of redshifts. Figure 3 compares the distributions of half-light radius, bulge fraction, magnitude, color and surface brightness for those galaxies in the photometric catalog population (6 GSS fields) to those with Keck redshifts. There are indeed no discernible differences between galaxies in the DEEP/GSS redshift sample and the photometric catalog population of the GSS fields. The bulge fraction distributions look nearly identical, and the color distributions also look similar.

Finally, and most importantly, the surface brightness distributions show that the galaxies with DEEP/GSS Keck redshifts are an unbiased sample of the surface brightnesses of the photometric catalog. A detailed analysis of the survey selection function is carried out in the next section.

2.3.2. Determination of the DEEP/GSS Selection Function for Disk-Dominated Galaxies

The observed distribution of galaxies in the $M_{B_0} - R_d$ plane as a function of redshift $\Psi(M_{B_0}, R_d, z)$ is the result of any inherent changes in the resident⁶ galaxy distribution $\Psi_U(M_{B_0}, R_d, z)$ in that plane and of observational selection effects. Selection effects are likely to be significant given the wide range of sizes and surface brightnesses observed locally (Bender, Burstein & Faber 1992, Burstein et al. 1997). It is therefore important to carefully characterize selection effects to disentangle them from real changes in $\Psi_U(M_{B_0}, R_d, z)$. The path from $\Psi_U(M_{B_0}, R_d, z)$ to $\Psi(M_{B_0}, R_d, z)$ is given by:

$$\Psi(M_{B_0}, R_d, z) = S_{PS}(M_{B_0}, R_d, z) S_{UP}(M_{B_0}, R_d, z) \Psi_U(M_{B_0}, R_d, z), \quad (5)$$

where M_{B_0} is the rest-frame B-band absolute magnitude and R_d is the disk scale length in kpc (note the use of lower and upper cases to distinguish between apparent and intrinsic radii throughout this paper). The subscript *UP* stands for “Universe to Photometric sample”, and the subscript *PS* stands for “Photometric sample to Spectroscopic sample”. The resident galaxy distribution $\Psi_U(M_{B_0}, R_d, z)$ is not known *a priori*. Once the two selection functions in Equation 5 have been characterized, their product (denoted S_{US} hereafter) shows the region of the $M_{B_0} - R_d$ plane where real galaxies would have been observed if they existed in that region at high redshift.

The selection function $S_{UP}(M_{B_0}, R_d, z)$ contains the information needed to go from any sample of galaxies on the sky to the photometric catalog produced with SExtractor and reflects the adopted SExtractor detection parameters (detection threshold in

⁶It is very important to note the use of the term “resident” here and throughout the rest of the paper to refer to the intrinsic galaxy population at a given redshift z . In the absence of real evolution in the galaxy population with redshift, all resident populations would be the same as the local population of galaxies.

sigmas, minimum detection area, etc.). In practice, $S_{UP}(M_{B_0}, R_d, z)$ is derived from the selection function $S_{UP}(I_{814}, r_d)$ determined as a function of the observed apparent magnitude I_{814} and the apparent disk scale length r_d in arcseconds. The transformation $S_{UP}(I_{814}, r_d) \rightarrow S_{UP}(M_{B_0}, R_d, z)$ was made in each redshift bin using k -corrections calculated with the median observed galaxy $V_{606} - I_{814}$ color of the $B/T \leq 0.2$ galaxies at that redshift and the assumed cosmology.

$S_{UP}(I_{814}, r_d)$ was constructed by generating 50,000 $B/T = 0$ galaxy models with structural parameter values uniformly covering the ranges: $16.0 \leq I_{814} \leq 25.0$, $0''.0 \leq r_d \leq 10''.0$, $0^\circ \leq i \leq 85^\circ$. Each model galaxy was added, one at a time, to an empty $20'' \times 20''$ section of a typical *HST* GSS image. “Empty” here means that no objects were detected by SExtractor in that sky section with the same detection parameters used to construct the object catalog. Using an empty section of the GSS ensured that $S_{UP}(I_{814}, r_d)$ was constructed with the real background noise that was seen by the detection algorithm. The background noise included read-out, sky and the brightness fluctuations of very faint galaxies below the detection threshold. This last contribution to the background noise is particularly hard to model theoretically, and the current approach bypassed this problem. SExtractor was run on each simulation with the same parameters that were used to build the SExtractor catalog. The function $S_{UP}(I_{814}, r_d)$ was taken to be the fraction of galaxies successfully detected and measured by SExtractor at each value of (I_{814}, r_d) .

The resulting $S_{UP}(I_{814}, r_d)$ is shown in the upper left-hand panel of Figure 4. Since the SExtractor detection algorithm depends mostly on surface brightness, it is easy to understand why $S_{UP}(I_{814}, r_d)$ is bounded at low surface brightness by a line of nearly constant surface brightness, i.e., a straight line in the $M_{B_0} - R_d$ plane with slope close to -5 . At the faint end, the boundary curves down as objects reach a total magnitude limit where they cannot meet the surface brightness detection threshold for any size. The upper center panel shows the magnitude distribution $\Psi_P(I_{814})$ of the general GSS population in the SExtractor catalog, and the upper right-hand panel shows the magnitude distribution $\Psi_S(I_{814})$ of galaxies with Keck redshifts. The lower left-hand panel of Figure 4 shows the second observed selection function, $S_{PS}(I_{814}, r_d)$ which is needed to go from the photometric catalog $\Psi_P(I_{814})$ to the spectroscopic sam-

ple $\Psi_S(I_{814})$. Even though the DEEP/GSS sample is statistically complete down to $I_{814} = 23.5$ (i.e., a redshift was obtained for every galaxy targeted spectroscopically), $S_{PS}(I_{814}, r_d)$ should not be expected to simply be a flat function down to that magnitude limit but will rather show a negative gradient since the fraction of galaxies in the photometric catalog targeted spectroscopically decreases with increasing magnitude. $S_{PS}(I_{814}, r_d)$ is computed in the observed $I_{814} - r_d$ plane according to the rules described in Appendix A and then transformed to the rest frame $S_{PS}(M_{B_0}, R_d, z)$ in each redshift bin with the same k -corrections as for $S_{UP}(I_{814}, r_d)$. Note that the cutoff at $I_{814} = 23.5$ has been applied. $S_{PS}(I_{814}, r_d)$ is flat at $I_{814} \leq 19.0$ since any galaxy above that magnitude limit would have been targeted spectroscopically.

The final selection function $S_{US}(I_{814}, r_d)$, which is the product of S_{UP} and S_{PS} , is shown in the lower right-hand panel of Figure 4. The apparent sizes and magnitudes of galaxies with Keck redshifts above $I_{814} = 23.5$ are also plotted over the filled contours of S_{US} . Note that the observed density of points does not necessarily follow the contours of S_{US} since bright galaxies, though they have a greater probability of being detected, are also less numerous in the Universe. The rest-frame counterparts of $S_{US}(I_{814}, \log r_d)$ at each redshift are presented in the next section in conjunction with the magnitude-size relation for disk galaxies as a function of redshift.

3. The Magnitude-Size Relation

3.1. Disk galaxies

Figure 5 shows the relation between intrinsic disk scale length and disk rest-frame absolute B-band magnitude as a function of redshift for galaxies with $B/T < 0.5$ in the DEEP/GSS sample. The redshift ranges of the lowest three bins are nearly identical to those of Schade et al. (1996a,b). However, the Keck sample goes 1.5–2.0 magnitudes deeper than their CNOC sample and also provides two bins at higher redshifts between $z = 0.70$ and $z = 1.10$. The error bars on the points are the 99% confidence intervals of the I_{814} and r_d measurements. The open triangles are objects with structural parameters measured with the same software as the rest of the objects but whose redshifts come from the CFRS survey. The redshift range covered by all five bins corresponds to a total lookback time interval of 5.8 Gyrs ($q_0 = 0.1$).

The long-dashed line is the Freeman relation for an

exponential disk B-band central surface brightness of $21.65 \text{ mag arcsec}^{-2}$ (Freeman 1970). The disk sizes and luminosities of most galaxies in the two lowest redshift bins cluster near this relation. Galaxies in the third redshift bin also cluster around the Freeman relation, although a substantial number of objects begin to exhibit systematically higher central surface brightness than the Freeman value. Major deviations from the Freeman relation are seen above $z = 0.70$, with evidence for a class of very small, high-surface brightness objects at $z \geq 0.90$. It is interesting to observe that a significant number of galaxies remain on the Freeman locus even at $z \geq 0.90$, consistent with the existence of a population of Freeman surface brightness disks even at this early epoch. The large spread in surface brightness at $z \geq 0.90$ may be due either to a strong differential disk evolution that leaves some galaxies unaffected or to a new galaxy population making its entrance at $z \geq 0.90$. Both possibilities are discussed further in Section 4.

The magnitude-size relations shown in Figure 5 cannot be properly interpreted without taking selection effects into account. In Figure 6, the rest-frame selection function S_{US} for each redshift bin is shown as the shaded contours, and the same galaxies as in Figure 5 are replotted to compare their location to the predictions of the selection function. The Freeman disk relation is also replotted for reference. Two important observations can be made from Figure 6. First, very few disks are observed at low redshifts in the ranges $-20 \leq M_{B_0}(\text{disk}) \leq -18$ and $0.5 \leq \log R_d \leq 1.2$ (significantly above the Freeman relation) even though they are detectable in principle. Second, the envelope of the selection function in the two highest redshift bins comes close to the Freeman locus, and this situation has a very serious implication: galaxies whose surface brightness may have been *fainter* at those redshifts are *not* detectable in the DEEP/GSS sample. Hence, this sample cannot be used to distinguish between a scenario in which mean surface brightness is higher at high redshift and one in which mean surface brightness remains unchanged but the *spread* in surface brightness about that mean value increases.

Although the present sample may be somewhat biased to high surface brightness at high redshift, this effect would appear to be even more pronounced in the Schade et al. (1996a,b) and Roche et al. (1998) samples. This is shown in Figure 7, which illustrates loci in the magnitude-size plane occupied by the vari-

ous samples as a function of redshift. The DEEP/GSS loci are taken from Figure 5 and are shown by the solid boxes. Loci for the other samples have been drawn by eye from analogous plots in the published papers. These boxes cannot substitute for a quantitative treatment, but even this rough comparison is instructive.

Systematically, it is seen that the loci of the Schade et al. and Roche et al. samples lie at higher surface brightness relative to the DEEP/GSS sample, and that this offset increases with redshift. Put differently, the first two samples fail to include many low surface brightness objects of the sort actually detected by DEEP/GSS. Quantitatively, at $z \sim 0.7$, the upper boundary difference between the first two samples and DEEP/GSS is about 0.3 dex in $\log R_d$. Loss of these galaxies would translate to a shift of about 0.75 mag in mean surface brightness if the DEEP/GSS box were uniformly populated vertically – about the same magnitude as the surface brightness evolution actually found in the other two samples. Figure 7 thus raises the possibility that the surface brightness evolution seen by Schade et al. and Roche et al. might have been caused in large part by the loss of low surface brightness objects at high z .

Figure 7 also shows boxes marking the distant compact galaxy sample of Phillips et al. (1997). This sample represents the top 35% of galaxies in surface brightness to $I_{814} = 23.5$ around the Hubble Deep Field. The location of the Phillips et al. sample in Figure 7 is consistent with its compact high surface brightness nature. Further comparison is made to this sample below.

As a first step to study in greater detail whether the magnitude-size relations shown in Figure 5 exhibit real evolution or not, surface brightness distributions were calculated for each redshift bin. The disk rest-frame B-band central surface brightness of each galaxy was computed using the relation:

$$\mu_{0_B} = M_{B_0} + 5.0 \log R_d + 38.57, \quad (6)$$

where M_{B_0} is the disk rest-frame B-band absolute magnitude, and R_d is the disk scale length in kpc. Equation 6 is valid for pure exponential disks, and the units of μ_{0_B} are mag arcsec^{-2} . The resultant surface brightness distributions shown in Figure 8 are raw without correction for selection effects, and the area under each distribution is normalized to unity. The mean of each distribution is shown as a large filled circle, and the error bar attached to each circle is 3

times the standard error of the mean. The vertical dotted lines mark the canonical Freeman disk central surface brightness of $21.65 \text{ mag arcsec}^{-2}$. There is a systematic increase in the mean disk central surface brightness from $\mu_{0_B} = 21.7 \text{ mag arcsec}^{-2}$ at $z = 0.20$ to $\mu_{0_B} = 20.4 \text{ mag arcsec}^{-2}$ at $z = 0.80$. This raw increase of 1.3 mag is similar to the effect seen by Schade et al. and Roche et al. over the same redshift range.

Next, the surface brightness distributions were recalculated by taking the survey selection function into account. Let $\phi_{ij}(\mu_{0_{B_{ij}}})d\mu_{0_{B_{ij}}}$ be the number of galaxies in the j^{th} bin of the surface brightness distribution for the i^{th} redshift bin. Adjusted surface brightness distributions in Figure 9 were calculated using the equation:

$$\phi_{ij}(\mu_{0_{B_{ij}}})d\mu_{0_{B_{ij}}} = \sum_k \frac{S_{US}(R_{d_{ijk}}, M_{ijk}, 0.90 \leq z)}{S_{US}(R_{d_{ijk}}, M_{ijk}, z_i)} \quad (7)$$

where the index k runs over all the galaxies in the i^{th} redshift bin with surface brightness between $\mu_{0_{B_{ij}}}$ and $\mu_{0_{B_{ij}}} + d\mu_{0_{B_{ij}}}$. Each object was thus de-weighted by the inverse ratio of the value of the selection function in its redshift bin and magnitude-size position to the value of the selection function in the highest redshift bin at the same magnitude-size position. This weighting scheme effectively applies the selection function of the highest redshift bin uniformly to all the redshift bins. The area under each distribution in Figure 9 was again normalized to unity. The parameters of the surface brightness distributions with and without selection function corrections are given in Table 1. These distributions show that there is *no* detectable systematic change in the mean disk central surface brightness over the redshift range $0.1 - 1.1$ when a uniform selection function is applied to all bins. Why has this occurred? Previous discussion hinted that loss of low surface brightness galaxies at high z might be important. However, the major consequence of applying the highest redshift selection function to all bins is actually the deletion of *intrinsically faint* galaxies below $M_{B_0} = -19 \text{ mag}$ from the nearer redshift bins. Inspection of Figure 6 shows that the remaining, brighter galaxies tend to lie *below* the Freeman relation, i.e., at higher surface brightness, at all redshifts. In other words, once comparison is restricted to galaxies of similar (i.e., bright) absolute magnitude, no significant evidence for evolution in mean

disk surface brightness remains, at least for galaxies in the range $M_{B_0}(\text{disk}) = -19$ to -22 mag .

3.2. Global Population

The analysis so far has been restricted to the disks of disk-dominated galaxies with $B/T < 0.5$. To extend the analysis to the whole distant galaxy population, a local magnitude-size relation must be chosen that covers as many local galaxies as possible. The choice of a local magnitude-size relation is clearly key to interpreting the relation at higher redshifts. Schade et al. (1996a,b) used fits to galaxies in the cluster Abell 2256 ($z = 0.06$) as a local reference. Roche et al. (1998) used a set of four galaxy type-dependent relations (Freeman, E/S0, Sab-Sbc, and Scd-Im). While these relations are useful, they do not represent very well the wide range of local galaxy photometric parameters over all Hubble types.

To broaden the approach, half-light radii R_{hl} are introduced as a measure of galaxy size. Half-light radii are available for all local Hubble types in quantity in the RC3 catalog. Specifically, the sample of 957 local galaxies extracted from the RC3 by Burstein et al. (1997; BBFN) is used here. Figure 10 shows half-light radius versus M_{B_0} for this sample. The data are divided into four broad morphological classes: ellipticals (E), early-type spirals (Sa-Sbc), late-type spirals (Sc-Sdm), and irregular galaxies (Sm-Irr). The Freeman relation is again shown as a reference (now expressed using half-light radius). This large dataset demonstrates how significant the total spread in the local magnitude-size relations is: $\sim 1.5 \text{ mag}$ for the bright ellipticals and $\sim 3.0 \text{ mag}$ for the late-type spirals. More significant is the fact that the different local Hubble types differ systematically in radius (and, therefore, in surface brightness) at a given absolute magnitude. Figure 10 shows that, at $M_{B_0} = -22 \text{ mag}$, bright Sa-Sc spirals are nearly 2 magnitudes brighter in mean surface brightness than ellipticals; however, at $M_{B_0} = -18 \text{ mag}$, they are 2 magnitudes dimmer; Sm and Irr galaxies at $M_{B_0} = -18$ are a further 0.5 magnitude dimmer yet than Sc's.

These systematic effects are of crucial importance in predicting what distant surveys will show. Suppose, for the sake of argument, that the distant galaxy population is the same as that seen locally. The distant selection function will then cut through the manifold of galaxies in different locations at different redshifts, turning up galaxies in proportion to their resident number densities at each redshift. At nearby

redshifts, the selection function will turn up dim but abundant Sm and Irr types. At distant redshifts, it will turn up a mixture of rarer but brighter E’s and early-type spirals. Mean surface brightness averaged over all detected galaxies will thus tend to “walk” from low to high values with distance, precisely as seen in the raw data in Figure 6. (It may even walk at fixed absolute magnitude, depending on the relative volume densities of different Hubble types and how their surface brightnesses differ at that particular magnitude.)

Finally, it should be stressed that the BBFN catalog in Figure 10 is *not* a volume-limited sample, nor does it fairly sample the full range in surface brightnesses seen locally, from high surface brightness starbursting HII and compact narrow emission-line galaxies on the one hand, to low surface brightness dwarf spheroidals on the other. Comparisons must therefore be made with caution, taking note of these deficiencies. These issues are discussed further below.

Measured half-light radii of all DEEP/GSS galaxies are plotted against total rest-frame B-band absolute magnitudes in Figure 11. Filled circles are disk-dominated galaxies ($B/T < 0.5$), and open circles are bulge-dominated galaxies. The solid line is the Freeman relation. Figure 11 again shows that a significant number of galaxies remain on or close to the Freeman relation at all redshifts, and further that such galaxies are largely disk-dominated. Bulge-dominated galaxies appear to lie at higher surface brightnesses than disk-dominated galaxies, especially at the highest redshifts.

To facilitate further comparison, Figure 12 directly overplots the distant half-light radii from Figure 11 on top of the total local catalog from Figure 10 (tiny dots). As expected, at low redshift, the DEEP/GSS sample is dominated by intrinsically faint but abundant late-type galaxies deep in the luminosity function. These galaxies are largely disk-dominated, with $B/T < 0.5$ (solid dots, Figure 11) and occupy the same magnitude-size locus as local Sm-Irr galaxies (Figure 10), which also have pure exponential profiles (Gallagher & Hunter 1984). The excellent agreement between the two loci is not surprising given the small difference in epochs between the two samples.

As redshift increases, the observed magnitude-size envelope begins to shift, both in surface brightness and also in absolute magnitude. However, out to $z = 0.70$, the projected distributions in the magnitude-size plane remain roughly consistent with those pre-

dicted by the local envelope. There may be a slight shift to higher surface brightness at $M_{B_0} \lesssim -20$ in the $z = 0.50\text{--}0.70$ bin, but the number of points is small. Overall, the impression is one of no great change from local galaxies out to $z = 0.70$.

Beyond $z = 0.70$, there is a hint of change. First, the range of surface brightnesses in the $z = 0.70\text{--}0.90$ bin appears to be larger than that seen locally, and a handful of very high surface brightness objects (HSBs hereafter) has appeared. The latter effect cannot be due to observational errors on the radii, as they are quite small (cf. Figure 5). Denoted by the open circles in Figure 12, these HSBs increase still further in number in the $z = 0.90\text{--}1.10$ bin, where objects distinctly more compact than the local BBFN sample are seen. Remarkably, HSBs span the whole range of bulge fractions and rest-frame colors and therefore may not be restricted to a single structural type.

HSBs aside, the bulk of galaxies at $z > 0.7$ are notable more for their resemblance to the local sample than for their differences. This statement is tentative, as no quantitative comparison has yet been made between the near and distant samples taking *resident local densities* of the various structural types properly into account. It is also conceivable that further differences will emerge once velocity widths are measured (a survey of these is in progress). For now, the present results suggest simply that no great global evolution has occurred in the surface brightnesses of luminous galaxies since $z \sim 1$. This conclusion is based on a considerably deeper and more complete sample than heretofore available, as Figure 7 shows.

Strictly speaking, one should also carry out selection function experiments on half-light radii of the various Hubble types, analogous to those carried out for disk radii in Figure 6. However, the main effect of these experiments for bright galaxies was to limit the sample in magnitude, not in surface brightness. Thus, neither the relative constancy in surface brightness nor the appearance of luminous high surface brightness galaxies are likely to stem from as-yet-uncalibrated selection effects.

4. Discussion

The inclusion of selection effects in the analysis of the disk galaxy magnitude-size relation at high redshift has led to a number of important results.

First, even though the DEEP/GSS survey goes nearly two magnitudes deeper than previous studies,

the faint envelope of the survey selection function in surface brightness approaches the local Freeman relation at redshifts greater than $z = 0.70$. This means that the magnitude-size relation of past and present samples cannot be used by itself to favor a scenario in which the mean surface brightness of disks brightens systematically with redshift over a scenario in which the spread in disk surface brightness increases. Although theoretical expectations for the characteristic surface brightness of “normal” bright disk galaxies are comparable to the canonical central Freeman value of 21.7 ± 0.3 mag arcsec $^{-2}$, the spread about that value could be as large as ± 3.4 mag depending on the range of disk masses and mass-to-light ratios (Dalcanton, Spergel & Summers 1997). The disks on the faint end of that surface brightness distribution would quickly be excluded from the DEEP/GSS and other samples at relatively low redshifts.

Second, selection effects produce an apparent systematic increase in disk mean surface brightness that, at first sight, looks like luminosity and/or size evolution (Figure 8). However, there is no such systematic increase below $z = 1.1$ when the selection function is used to weigh the disk surface brightness distributions as a function of redshift. According to the selection function S_{US} , disks with absolute magnitudes brighter than $M_{B_0} = -19$ remain detectable over all redshift bins, and these are the disks that effectively contribute to the weighted surface brightness distributions. Significant evolution in the surface brightness of such disks is not apparent, though the numbers are still small. Selection effects are too important for fainter disks to determine whether or not their surface brightness is evolving with redshift.

Third, it is apparent from Figures 5 and 11 that a significant number of galaxies remain close to the canonical Freeman relation at all redshifts. This population may be the same as that detected in the Tully-Fisher zeropoint studies of distant galaxies by Vogt et al. (1996,1997). The Vogt galaxies were selected to include the largest (i.e., best resolved) morphologically normal spirals at each apparent magnitude, a criterion that favors lower surface brightness galaxies in each redshift bin. It is probable that the Vogt et al. studies also targeted late-type spirals preferentially, since they have stronger emission lines. The constancy of the TF zeropoint for these particular objects would then not be surprising, since the star-formation timescales of late-type galaxies are quite long ($\tau_{SFR} \geq 7$ Gyrs, Bruzual & Charlot 1993), and

mass-to-light ratios for such stellar populations evolve only slightly.

These long timescales are a feature of the Pure Luminosity Evolution model of Roche et al. (1998), which predicts that the surface brightness of late-type spirals should remain constant out to $z = 1$. On the other hand, their Size-Luminosity Evolution model predicts that the same late-type galaxies should increase nearly 1.5 magnitudes in surface brightness to the same redshift (Figure 7, Roche et al. 1998). This latter model does not appear to be consistent with the DEEP/GSS data. Indeed, according to Figure 11, such a large brightening, if present in all disk galaxies, would considerably decrease the number of galaxies on the Freeman relation. This deficiency of galaxies on the Freeman relation could not be compensated by increasing the surface brightness of any resident Irr population, even if present. The internal kinematics of Irr galaxies cannot reproduce the observations of Vogt et al. The most massive Irr galaxies have rotation velocities lower than 100 km s $^{-1}$, and typical Irr galaxies have $V_c \sim 50 - 70$ km s $^{-1}$ (Gallagher & Hunter 1984).

As noted earlier, the last redshift bin ($z \geq 0.9$) contains about nine luminous, high surface brightness (HSB) objects (shown as open circles in Figure 12) that occupy a region of the magnitude-size plane rarely populated by local galaxies. The exact number of these aberrant objects depends on the boundary adopted for the envelope of normal local galaxies; a conservative, high surface brightness boundary was adopted here, minimizing the number of HSBs. The nature of the HSBs will be the subject of a future paper. For now, it is sufficient to note that the present HSBs occupy essentially the same region of the magnitude-size plane as the distant compact sample of Phillips et al. (1997), as shown in Figure 7. Like the present HSBs, that sample exhibited a mixture of colors and emission-line strengths, and many also had structural parameters similar to the distant compact narrow emission-line galaxies of Guzmán et al. (1998). Based on colors and spectra, Phillips et al. concluded that their population of HSBs was rather heterogeneous, though with a tendency to low internal velocity widths compared to local galaxies of similar absolute magnitude. The present data give further support to the notion that HSBs are a mixed population. Furthermore, it is also worth noting that the magnitude-size locus of the $z \sim 3$ galaxies observed by Lowenthal et al. (1997) overlaps with some HSBs

(see dashed box in Figure 12). Although this overlap raises interesting possibilities, it is by itself insufficient to directly link some HSBs to $z \sim 3$ galaxies. Potential links between these two types of galaxies will be explored in a future paper using a full set of structural parameters and emission linewidths.

At least three explanations for HSBs suggest themselves: (1) They may represent an entirely new population of galaxies not found locally and making its appearance at $z \sim 1$. (2) The local magnitude-size dataset used as a comparison here may be incomplete. Indeed, BBFN warn that rare types of local HSB galaxies such as starburst HII galaxies may be missing from their sample. The blue colors of some HSBs strongly suggest that at least some are starbursts. (3) HSB galaxies may have had high surface brightness in the past but have faded to become a normal population locally. For example, at a fixed radius, most HSB galaxies would have to fade by at least 1 mag to fall within the local magnitude-size envelope today. This is consistent with the passive evolution of a very early-type population, and it would nicely explain red HSBs. In view of the heterogeneous nature of HSBs, all three scenarios may be at work.

5. Conclusions

The *HST* structural parameters of 190 galaxies ($I_{814} \leq 23.5$) in the Groth Survey Strip with DEEP Keck redshifts have been used to build a magnitude-size relation in five redshift bins over the range $0.10 \leq z \leq 1.10$. Selection functions were quantitatively determined for all five redshift bins. The major conclusions are:

1. If selection effects are ignored, the mean surface brightness of disks in the sample appears to increase systematically by ~ 1.3 mag from $z = 0.1$ to $z = 0.9$. Such an increase was also found by Schade et al. (1996b) and Roche et al. (1998).

2. However, if the survey selection functions are used to correct the surface brightness distributions in the different redshift bins, then there is *no* detectable change out to $z = 0.9$ in the mean surface brightness of disks brighter than $M_{B_0} = -19$. These disks are the faintest objects not significantly affected by selection effects in the highest redshift bin.

3. A number of disks remain on the canonical Freeman relation in all redshift bins. This is consistent with the lack of evolution seen in the zero-

point of the high-redshift Tully-Fisher relation of Vogt et al., and it does not support a 1.5 mag brightening in surface brightness predicted for *all* late-type galaxies by the Size-Luminosity Evolution model of Roche et al. (1998). On the other hand, the constant surface brightness of late-type galaxies predicted by their Pure Luminosity Evolution model agrees with the DEEP/GSS observations of these disks.

4. At all redshifts, two important factors conspire to produce an apparent increase in global galaxy surface brightness out to $z = 0.9$: the relative volume densities of different Hubble types and the survey selection function. Lower surface brightness late-type and irregular galaxies will dominate lower redshift bins due to their higher volume densities. Higher surface brightness early-type galaxies will dominate the highest redshift bins as a result of increasing survey volume and the selection function cutting different slices through the resident galaxy surface brightness distribution at that redshift. So, for example, even if the distant galaxies were identical to those seen locally, average galaxy surface brightness would still shift to higher values at higher redshifts, in qualitative agreement with what is seen. Systematic shifts in galaxy surface brightness versus redshift thus may not necessarily represent real evolution in the radii or luminosities of the resident galaxy population.

5. Nine galaxies at redshifts $z \gtrsim 0.9$ occupy a region of the magnitude-size plane rarely populated by local galaxies. As will be shown in a forthcoming paper, these luminous, high surface brightness galaxies exhibit a wide range of rest-frame colors and bulge fractions. This suggests that a variety of scenarios might be required to explain their origin: a new population at $z \sim 1$ not found locally, a rare population missed by local surveys, and/or a familiar local population that has faded by at least 1 mag from $z \sim 1$ to the present epoch.

Further work is needed to fully understand the magnitude-size relation of the global galaxy population out to $z \sim 1$. Prime requirements are a truly volume-limited sample of local galaxies plus comoving volume densities for the distant samples. The size of the distant sample must also be increased to study the statistical properties of the HSB population and determine its origin. Finally, linewidths must be obtained to provide full structural information, including masses. These additional parts of the global structural puzzle will be tackled in future papers.

Caryl Gronwall kindly provided the model SEDs and the code used for the k -corrections. This work was funded by NSF grants AST 91-20005 and AST95-29098 and NASA grants AR-06337.08-94A, AR-06337.21-94A, AR-06402.01-95A, AR-07531.01-96A and AR-07532.01-96A. L. S. gratefully acknowledges financial support from a Postdoctoral Fellowship from the Natural Sciences and Engineering Research Council of Canada. David Burstein kindly provided an electronic copy of the BBN database. Thanks go to J. Cohen and B. Oke for building the LRIS spectrograph. Many thanks also go to the Keck telescope operators and staff for their dedication and hard work in the harsh environment of the Mauna Kea summit.

REFERENCES

- Andredakis, Y. C. 1998, MNRAS, 295, 725
- Bender, R., Burstein, D., & Faber, S.M. 1992, ApJ, 399, 462
- Bertin, E., & Arnouts, S. 1996, A&AS, 117, 393
- Bouwens, R. J., Cayón, L., & Silk, J. 1997, ApJ, 489, 21
- Bruzual A., G., & Charlot, S. 1993, ApJ, 405, 538
- Burstein, D., Bender, R., Faber, S. M., & Nolthenius, R. 1997, AJ, 114, 1365
- Cayón, L., Silk, J., & Charlot, S. 1996, ApJ, 467, 53
- Chiappini, C., Matteucci, F., & Gratton, R. 1997, ApJ, 477, 765
- Contardo, G., Steinmetz, M., & Fritze-von Alvensleben, U. 1998, astro-ph/9801278
- Courteau, S., de Jong, R. S., & Broeils, A. H. 1996, ApJ, 457, 73
- Dalcanton, J., Spergel, D. N., & Summers, F. J. 1997, ApJ, 482, 659
- de Jong, R. S. 1994, Ph. D. Thesis, Leiden, Netherlands
- Firmani, C., & Avila-Reese, V. 1998, astro-ph/9803090
- Freeman, K. C. 1970, ApJ, 160, 811
- Gallagher, J. S., III, & Hunter, D. A. 1984, ARA&A, 22, 37
- Guzmán, R., Jangren, A., Koo, D. C., Bershad, M., & Simard, L. 1998, ApJ, 495, 13
- Koo, D. C. 1998, in Proceedings of IAU 23 Joint Discussion 11: "Redshift Surveys in the 21st Century", ed. A. P. Fairall (Dordrecht:Kluwer)
- Kormendy, J. 1985, ApJ, 295, 73
- Krist, J. 1993, in Astronomical Data Analysis Software and Systems II, 52, eds. Hanisch, R. J., Brinsenden, R. J. V., and Barnes, J. (A.S.P. Conference Series), p. 536
- Lilly, S. J., Tresse, L., Hammer, F., Crampton, D., & Le Fèvre, O. 1995, ApJ, 455, 108
- Lilly, S. J., Schade, D., Ellis, R., Le Fèvre, O., Brinchmann, J., Tresse, L., Abraham, R., Hammer, F., Crampton, D., Colless, M., Glazebrook, K., Mallen-Ornelas, G., & Broadhurst, T. 1998, ApJ, 500, 75
- Lin, D. N. C., & Faber, S. M. 1983, ApJ, 266, 17
- Lowenthal, J. D., Koo, D. C., Guzmán, R., Gallego, J., Phillips, A. C., Faber, S. M., Vogt, N. P., Illingworth, G. D., & Gronwall, C. 1997, ApJ, 481, 673
- Marleau, F. R., & Simard, L. 1998, ApJ, 505, 585.
- Metropolis, N., Rosenbluth, A., Rosenbluth, M., Teller, A., & Teller, E. 1953, Journal of Chemical Physics, 21, 1087
- Mo, H. J., Mao, S., & White, D. M. 1998, MNRAS, 295, 319
- Mao, S., Mo, H. J., & White, D. M. 1998, MNRAS, 297, 71
- Oke, J. B., Cohen, J. G., Carr, M., Cromer, J., Dingizian, A., Harris, F. H., Labrecque, S., Lucinio, R., Schall, W., Epps, H., & Miller, J. 1995, PASP, 107, 375
- Phillips, A. C., Guzmán, R., Gallego, J., Koo, D. C., Lowenthal, J. D., Vogt, N. P., Faber, S. M., & Illingworth, G. D. 1997, ApJ, 489, 543
- Roche, N., Ratnatunga, K., Griffiths, R. E., Im, M., & Naim, A. 1998, MNRAS, 293, 157
- Saha, P., & Williams, T.B. 1994, AJ, 107, 1295
- Schade, D., Carlberg, R. G., Yee, H. K. C., & López-Cruz, O. 1996a, ApJ, 464, 63
- Schade, D., Carlberg, R. G., Yee, H. K. C., & López-Cruz, O. 1996b, ApJ, 465, 103
- Simard, L. 1998 in Astronomical Data Analysis Software Systems VII, 145, eds. Albrecht, R., Hook, R. N. and Bushouse, H. A. (A.S.P. Conference Series), p. 108
- Vogt, N. P., Forbes, D. A., Phillips, A. C., Gronwall, C., Faber, S. M., Illingworth, G. D., & Koo, D. C. 1996, ApJ, 465, 15
- Vogt, N. P., Phillips, A. C., Faber, S. M., Gallego, J., Gronwall, C., Guzmán, R., Illingworth, G. D., Koo, D. C., & Lowenthal, J. D. 1997, ApJ, 479, 121

Fig. 1.— *Upper Panel*: $55'' \times 45''$ section of a typical WFPC2/F814W GSS image before GIM2D processing. Exposure time was 4400s. Galaxies in this image section span a wide range of bulge fractions. *Lower Panel*: GIM2D residual galaxy image of the same image section as shown above. GIM2D produced this residual image by subtracting the best bulge+disk surface brightness model from each galaxy detected by SExtractor.

Fig. 2.— Examples of GIM2D surface brightness fits for a set of five galaxies covering a range of bulge fractions and redshifts. The left-hand panels are the original F814W galaxy postage stamp images analyzed by GIM2D, the central panels are the PSF-convolved best fitting surface brightness models, and the right-hand panels are the residual images. Redshift and measured bulge fraction are given for each object. These five galaxies have $19.9 \leq I_{814} \leq 22.3$.

Fig. 3.— Observed structural parameter distributions for galaxies with DEEP Keck redshifts (*solid line*) and for an identically selected sample of galaxies in the general GSS population (*dotted line*). From left to right and from top to bottom: PSF-deconvolved half-light radius r_{hl} , observed F814W bulge fraction B/T , F814W total magnitude I_{814} , total $V_{606} - I_{814}$ galaxy color, observed F814W effective surface brightness μ_{e814} in mag arcsec $^{-2}$. Magnitudes and colors are in the Vega zeropoint system. The spectroscopic sample shares the same characteristics as the general field population.

Fig. 4.— *From left to right and from top to bottom*: SExtractor selection function $S_{UP}(I_{814}, r_d)$, magnitude distribution $\Psi_P(I_{814})$ of galaxies in the photometric catalog, magnitude distribution $\Psi_S(I_{814})$ of galaxies in the spectroscopic catalog, Keck spectroscopic selection $S_{PS}(I_{814}, r_d)$, and combined survey selection function $S_{US}(I_{814}, r_d)$. The highest contour was normalized to one in each case. The red points in the bottom right-hand panel are the galaxies with Keck redshifts in the sample. The observed distribution of galaxies in the $I_{814} - r_d$ plane is given by the resident galaxy distribution in that plane multiplied by $S_{US}(I_{814}, r_d)$. The solid line in the upper left-hand panel is an arbitrary line of constant apparent surface brightness.

Fig. 5.— Disk scale length versus disk rest-frame B-band absolute magnitude as a function of redshift for

galaxies with $B/T < 0.5$. *Filled circles*: Galaxies with Keck redshifts; *Open triangles*: Galaxies with CFRS redshifts. *Long-dashed line*: Canonical Freeman relation for a disk central surface brightness $\mu_{0B} = 21.65$ mag arcsec $^{-2}$ (Freeman 1970). Error bars are 99% confidence intervals. The lowest three redshift bins cover nearly the same redshift ranges as those in Schade et al. (1996b). The loci of the DEEP/GSS galaxies (*solid outlines*) are used later in the comparison with other samples (Section 3.1 and Figure 7).

Fig. 6.— Rest-frame selection function $S_{US}(M_{B_0}, R_d)$ (*shaded contours*) as a function of redshift. The highest contour was normalized to one in each redshift bin. Red symbols are galaxies from Figure 5 with Keck redshifts and $B/T < 0.5$, and the solid green line is the canonical Freeman relation.

Fig. 7.— Loci of different magnitude-size samples: DEEP/GSS (*solid outline*), Schade et al. (1996b) (*dotted outline*), Roche et al. (1998) (*dashed outline*), and Phillips et al. (1997) (*dot-dashed outline*). The DEEP/GSS outlines are the same as those shown in Figure 5. Note that the DEEP/GSS sample penetrates to lower surface brightnesses at high redshift than the other samples.

Fig. 8.— Raw disk rest-frame B-band central surface brightness distributions as a function of redshift uncorrected by the survey selection function S_{US} . Surface brightnesses were computed using Equation 6. The area under each distribution was normalized to one, and the vertical dashed lines mark the value of the canonical Freeman disk central surface brightness ($\mu_{0B} = 21.65$ mag arcsec $^{-2}$). The large filled circles give the location of the mean surface brightness in each redshift bin. The error bar on the location of the mean is the 3-sigma standard error. The mean surface brightness increases systematically from $\mu_{0B} = 21.7$ mag arcsec $^{-2}$ at $z = 0.2$ to $\mu_{0B} = 20.4$ mag arcsec $^{-2}$ at $z = 0.80$, similar to that seen by Schade et al. and Roche et al.

Fig. 9.— Adjusted disk rest-frame B-band central surface brightness distributions as a function of redshift scaled by the survey selection function S_{US} following Equation 7. This scaling converts each distribution to what it would look like if observed with the same selection function as the highest redshift bin. Each galaxy thus contributes the frac-

tion $S_{US}(R_{d_{ijk}}, M_{ijk}, 0.90 \leq z) / S_{US}(R_{d_{ijk}}, M_{ijk}, z_i)$ to these adjusted distributions. N_{gal} is the number of galaxies in each bin for which $S_{US}(R_{d_{ijk}}, M_{ijk}, 0.90 \leq z) \neq 0$. The vertical dashed lines mark the value of the canonical Freeman disk central surface brightness ($\mu_{0B} = 21.65$ mag arcsec $^{-2}$). The large filled circles give the location of the mean surface brightness in each redshift bin. The error bar is the 3-sigma standard error on the mean. There is no systematic increase in the mean surface brightness from $z = 0.2$ to $z = 0.8$. This shows how important selection effects can be in interpreting the magnitude-size relation at high redshift. A significant fraction ($\sim 25\%$) of galaxies in the highest redshift bin remained close to the Freeman canonical surface brightness of $\mu_{0B} = 21.65$ mag arcsec $^{-2}$.

Fig. 10.— Half-light radius and total rest-frame B magnitude data for 957 galaxies taken from Burstein et al. (1997) and Bender et al. (1992). Upper left-hand panel: ellipticals E (*filled circles*) and dwarf ellipticals dE (*open circles*). Upper right-hand panel: Sa (*filled circles*), Sab-Sb (*open circles*) and Sbc (*pluses*). Lower left-hand panel: Sc (*filled circles*) and Scd-Sdm (*open circles*). Lower right-hand panel: Sm (*filled circles*) and Irr (*open circles*). The solid line is the half light radius-magnitude relation for a canonical Freeman disk with a central surface brightness of 21.65 mag arcsec $^{-2}$. The Freeman relation is provided for the E galaxies only as a reference since, strictly speaking, it applies only to disk galaxies.

Fig. 11.— Half-light radius in kiloparsecs versus total rest-frame B-band absolute magnitude as a function of redshift for all galaxies with Keck redshifts. *Filled circles*: $0.0 \leq B/T < 0.5$, *Open circles*: $0.5 \leq B/T \leq 1.0$. The solid line is the half-light radius-magnitude relation for a canonical Freeman disk with a central surface brightness of 21.65 mag arcsec $^{-2}$.

Fig. 12.— Direct half-light radius-magnitude comparison between local BBFN galaxies (dots) and galaxies in the DEEP/GSS redshift sample (filled circles). The HSB galaxies are shown as open circles. The dashed box outlines the magnitude-size locus of the $z \sim 3$ galaxies from the sample of Lowenthal et al. (1997), and the solid line is the Freeman relation. Comparison with Figure 10 shows that the DEEP/GSS sample probably includes different morphological mixtures in different redshift bins, ranging from Sm-Irr galaxies at low redshift to early-type and HSB galaxies at high

redshift.

TABLE 1
 REST-FRAME SURFACE BRIGHTNESS DISTRIBUTION PARAMETERS

z	No Selection Function Adjustment			With Selection Function Adjustment		
	N_{gal}	$\bar{\mu}_{0B}$	$\sigma(\mu_{0B})$	N_{gal}	$\bar{\mu}_{0B}$	$\sigma(\mu_{0B})$
$0.10 \leq z < 0.30$	17	21.7 ± 0.3	1.2	5	20.3 ± 0.6	1.3
$0.30 \leq z < 0.50$	18	21.0 ± 0.3	1.2	6	20.2 ± 0.2	0.6
$0.50 \leq z < 0.70$	27	20.7 ± 0.2	0.8	14	20.3 ± 0.2	0.8
$0.70 \leq z < 0.90$	33	20.4 ± 0.2	1.1	31	20.2 ± 0.2	1.2
$0.90 \leq z < 1.10$	41	19.9 ± 0.2	1.4	41	19.9 ± 0.2	1.4

A. APPENDIX A: Rules for the Spectroscopic Selection Function S_{PS}

Ideally, $S_{PS}(I_{814}, r_d)$ should just be the ratio of the spectroscopic and photometric samples binned in both magnitude *and* size. Unfortunately, this is not always the case for two reasons. First, even with large bin sizes ($\Delta mag = 1.0$ and $\Delta \log r_d = 0.5$), small-number statistics at the bright end cause large fluctuations in $S_{PS}(I_{814}, r_d)$ where it should have been flat and close to its maximum value. To alleviate this small-number problem, the spectroscopic and photometric samples were binned only in magnitude ($\Delta mag = 1.0$). The resulting $S_{PS}(I_{814}, r_d)$ selection function is thus insensitive to any size-dependent effect in the spectroscopic selection. This would be a problem if the size distributions of galaxies in the spectroscopic sample were markedly different from those of the general population as a function of magnitude. No difference was found in four magnitude ranges: $20.5 \leq I_{814} < 21.5$, $21.5 \leq I_{814} < 22.5$, $22.5 \leq I_{814} < 23.5$, and $23.5 \leq I_{814} < 24.5$. Second, the ratio Ψ_S/Ψ_P of the spectroscopic and photometric samples must be calculated in each bin in the I_{814} – $\log r_d$ plane according to the rules shown in Table A2. Table A2 describes all the different ways in which the selection functions operate on Ψ_U and Ψ_P to produce Ψ_S . “Y” and “N” are used to indicate whether galaxies in the magnitude-size bin are present or not in the Ψ 's. For simplicity, zeroes and ones are used for the selection functions. In reality, they can obviously take on any value between 0 and 1 since they give the probabilities of detecting objects photometrically and spectroscopically.

Cases (3) and (7) are the only two cases where S_{PS} is greater than S_{UP} . These cases represent serendipitous observations of very strong emission-line objects which are not detected on broad-band images. Since these objects were not included in the spectroscopic sample used for this paper, Cases (3) and (7) do not apply here. S_{PS} must be carefully interpreted when both Ψ_P and Ψ_S are zero. Take Case (5) for example. Objects in this case are absent from both Ψ_P and Ψ_S because they do not exist in Universe and not because they could not have been detected in principle. It would therefore be wrong to set S_{PS} to zero if these selection functions were to be applied to predictions from theoretical models. The selection functions should not erase potential differences between theoretical model predictions and the true galaxy population in the Universe. The best estimate for S_{PS}

in this case is therefore an upper limit given by the value of S_{UP} in the same magnitude-size bin. Therefore, S_{PS} was set to S_{UP} whenever both Ψ_P and Ψ_S were zero. Otherwise, S_{PS} was simply set equal to Ψ_S/Ψ_P .

The selection rules discussed so far in this Appendix apply to the very general case of a survey in which redshifts may not have been obtained for all the objects observed and in which redshifts may have been obtained serendipitously for objects absent from its photometric catalog. The DEEP/GSS sample ($I_{814} \leq 23.5$) used in this paper was much simpler to analyze than such a general survey since Keck redshifts were obtained for 100% of the objects in the sample, and all objects were present in the DEEP/GSS photometric catalog. In this case, the spectroscopic selection function S_{PS} in a given (I_{814}, r_d) bin is simply the ratio of the number of galaxies observed spectroscopically and the number of galaxies in the photometric sample.

TABLE A2
SPECTROSCOPIC SELECTION FUNCTION S_{PS} RULES

Case	Universe Ψ_U	S_{UP}	Photometric Catalog Ψ_P	S_{PS}	Spectroscopic Catalog Ψ_S
1	Y	1	Y	1	Y
2	Y	1	Y	0	N
3	Y	0	N	1	Y
4	Y	0	N	0	N
5	N	1	N	1	N
6	N	1	N	0	N
7	N	0	N	1	N
8	N	0	N	0	N

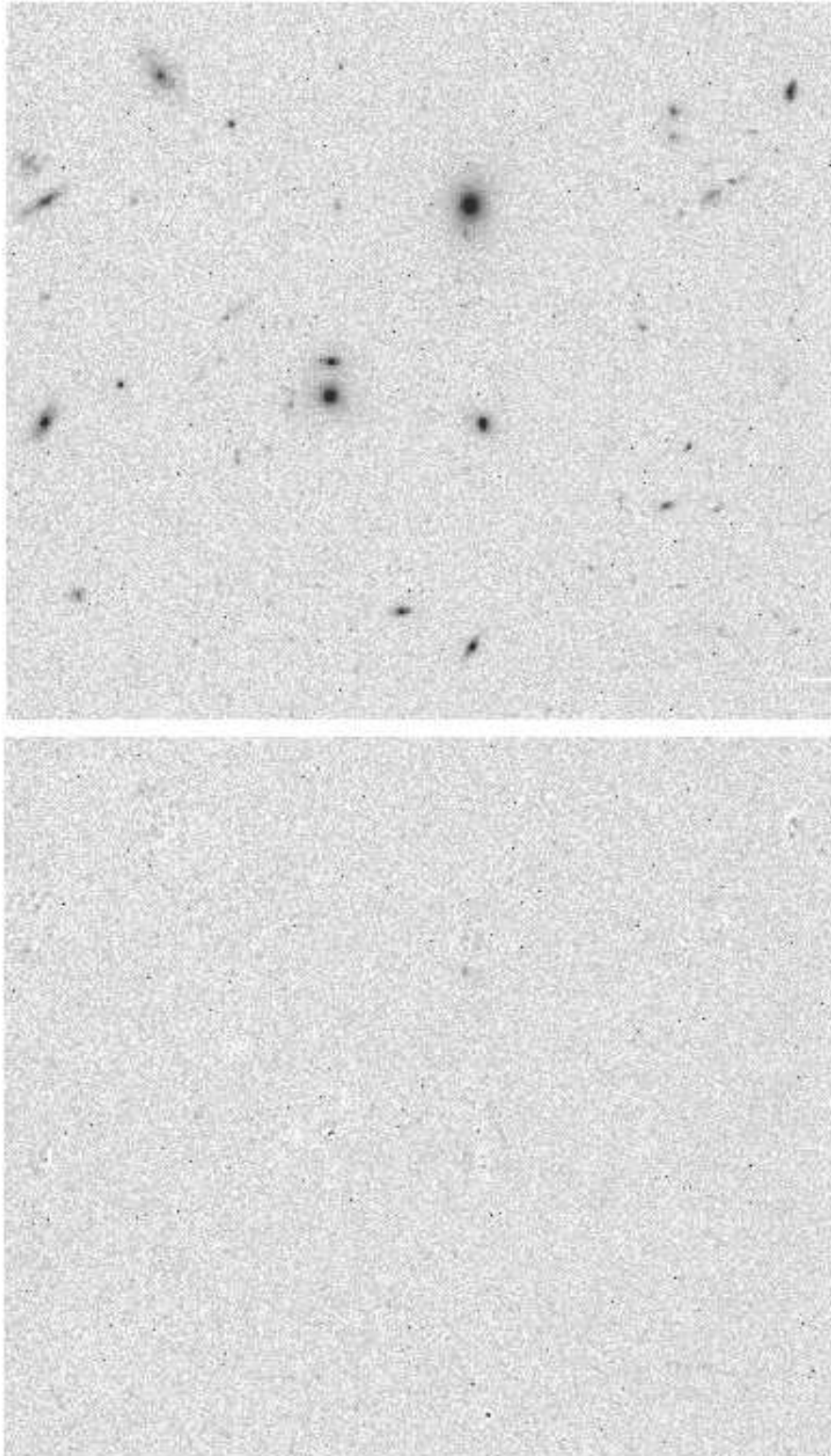
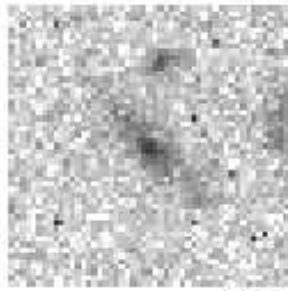
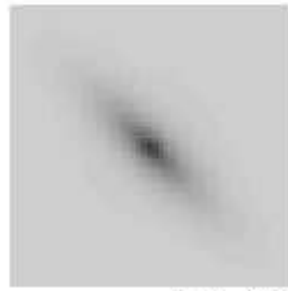


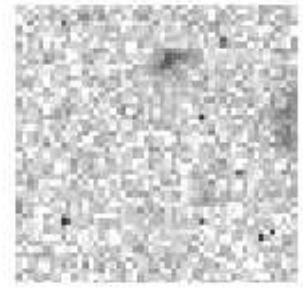
Figure 1.



$z = 0.9877$



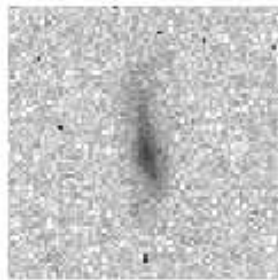
$B/T = 0.28$



$z = 0.6839$



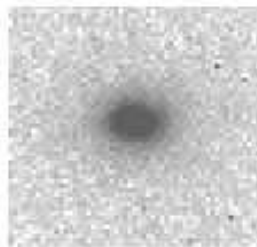
$B/T = 0.49$



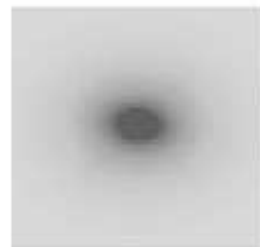
$z = 0.2661$



$B/T = 0.01$



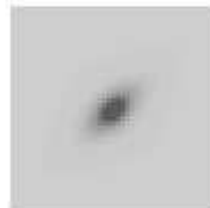
$z = 0.4635$



$B/T = 0.76$



$z = 0.8033$



$B/T = 0.97$



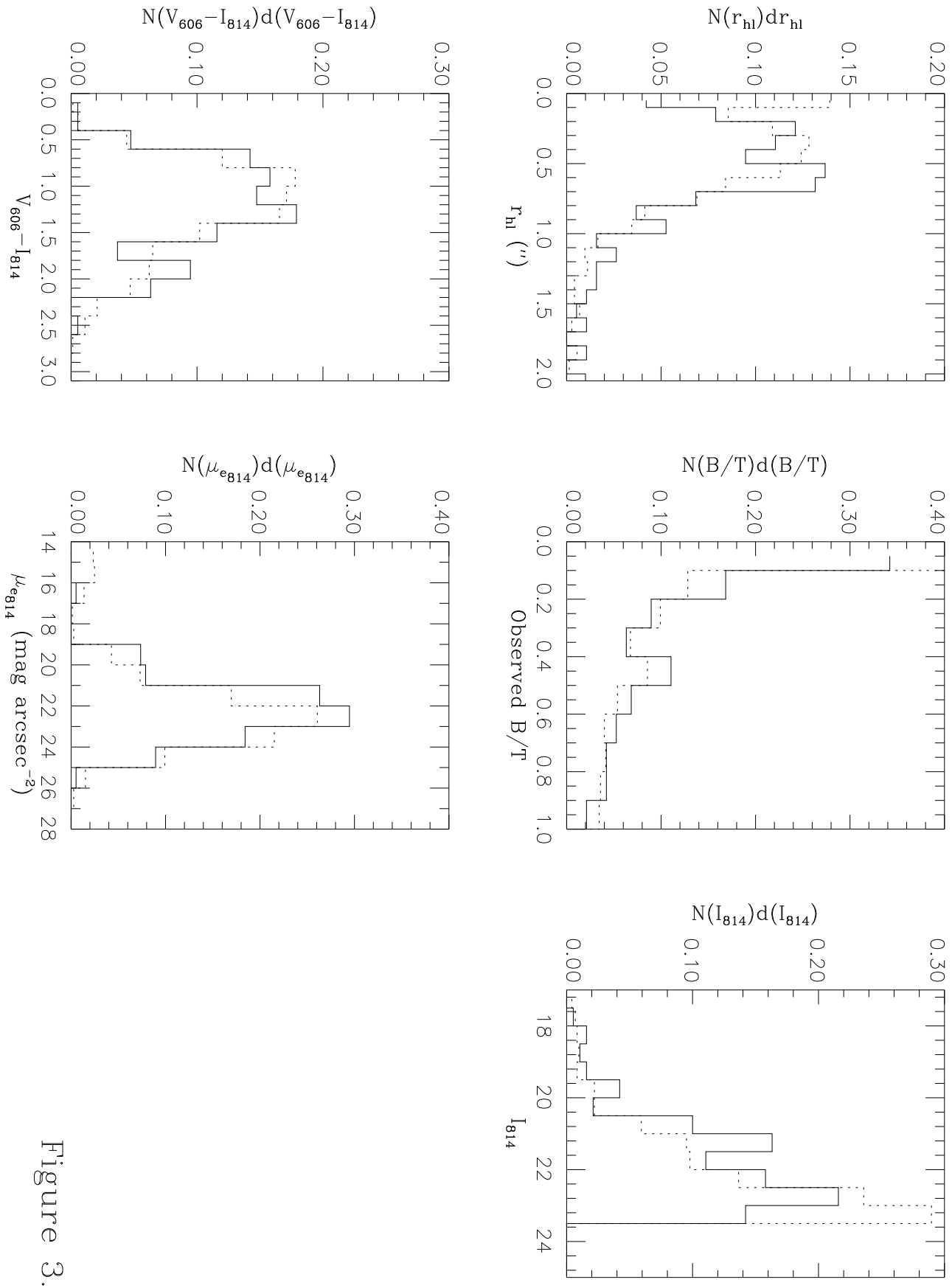


Figure 3.

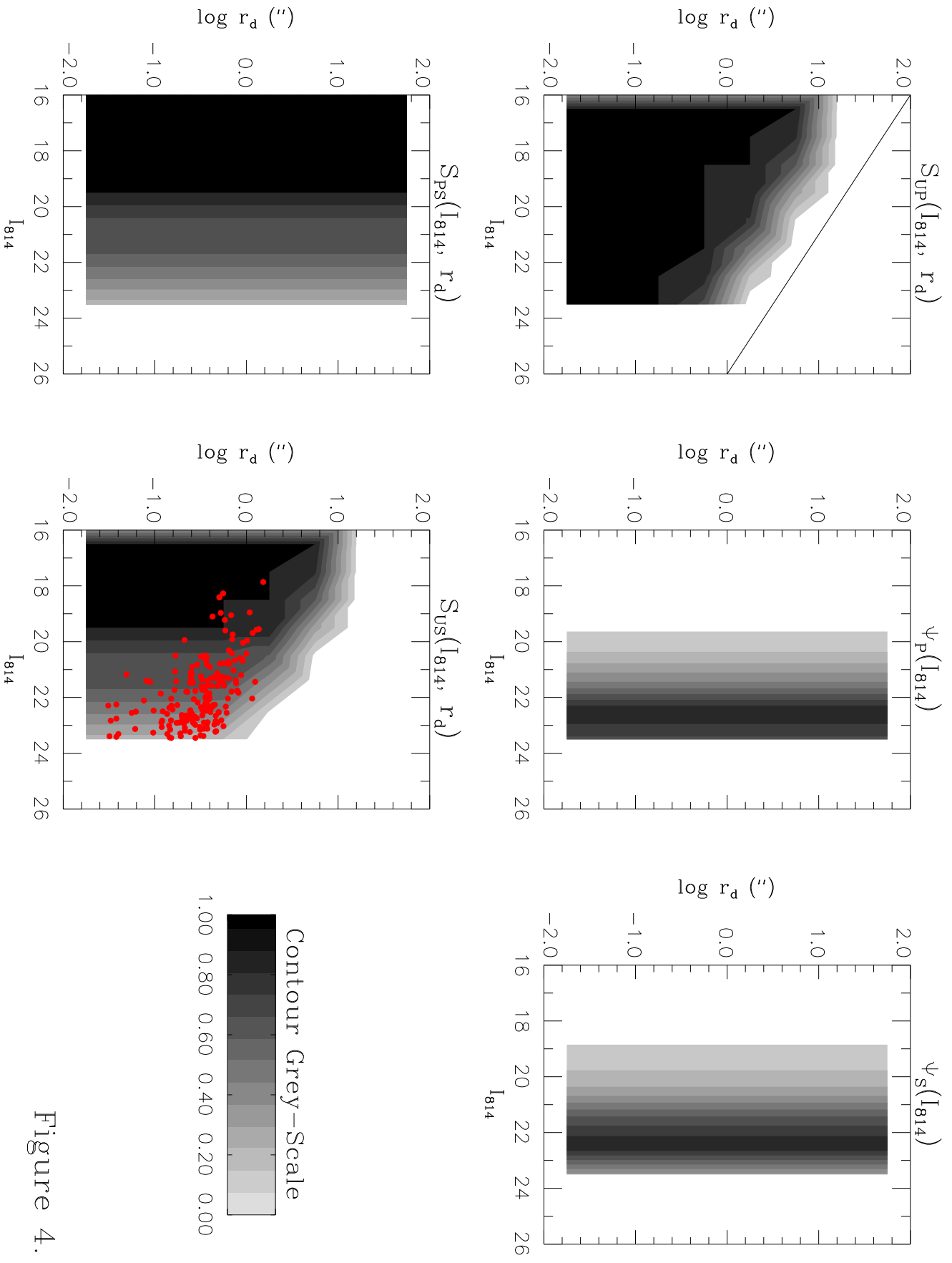


Figure 4.

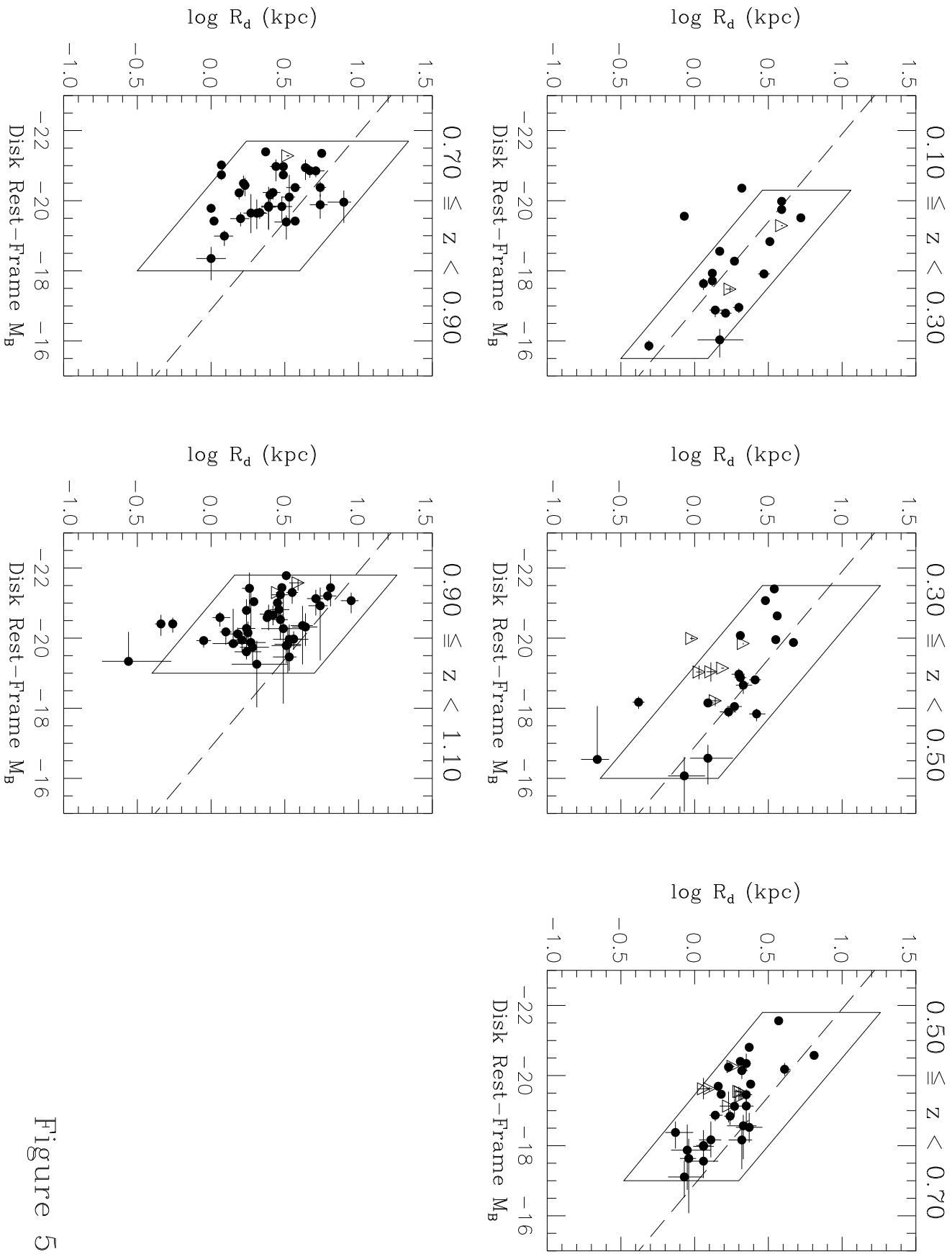


Figure 5.

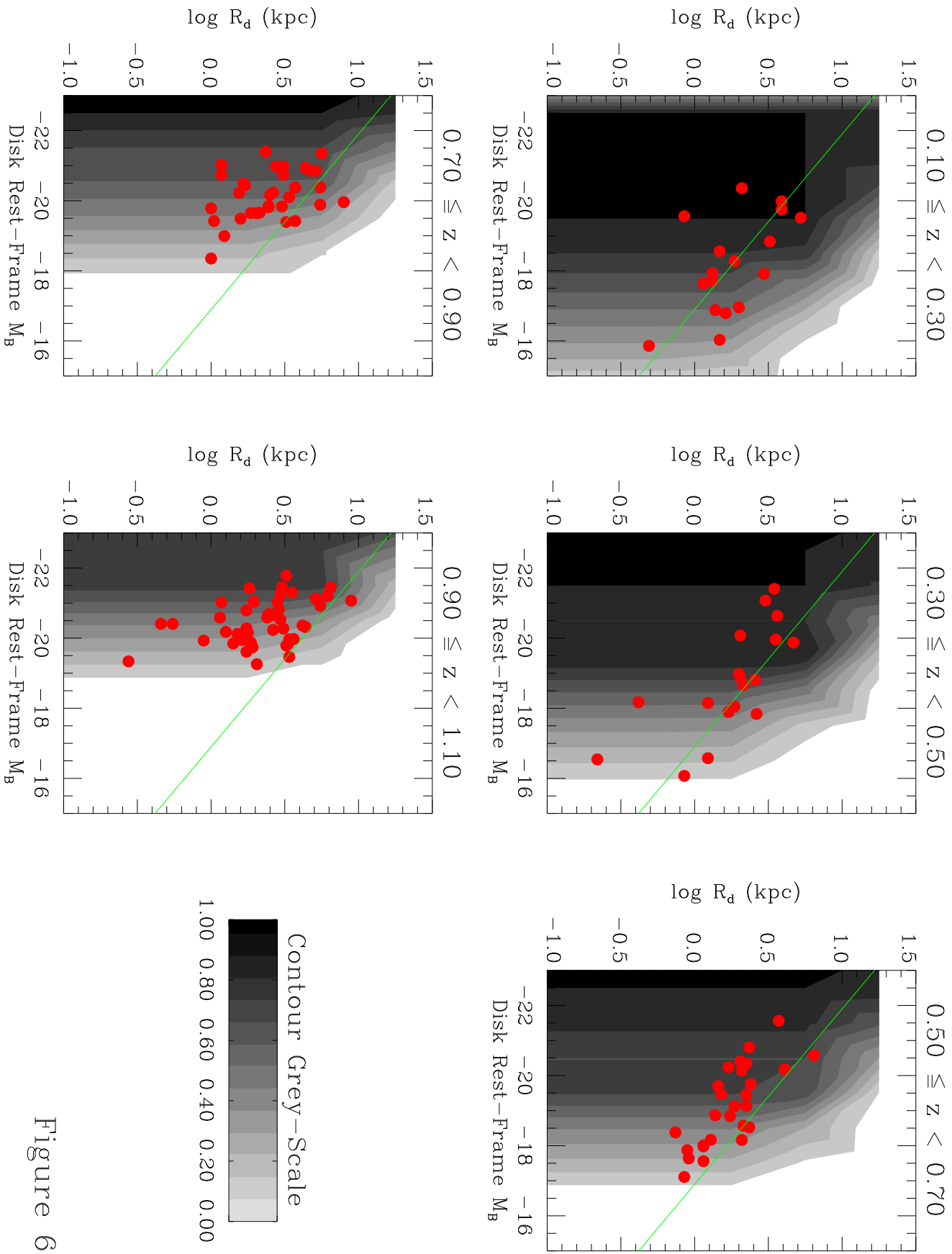
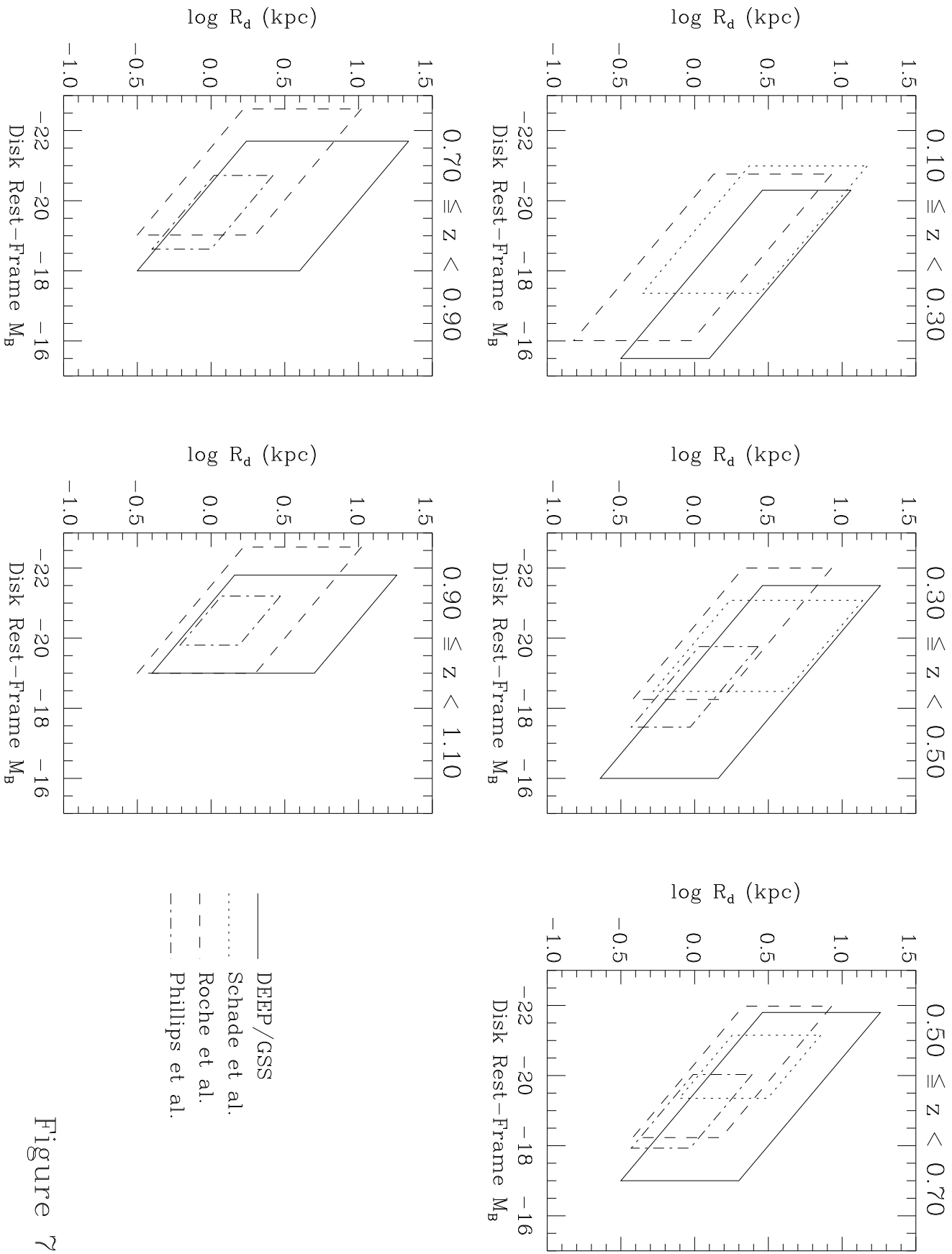


Figure 6.



— DEEP/GSS
 Schade et al.
 - - - Roche et al.
 - · - · - Phillips et al.

Figure 7.

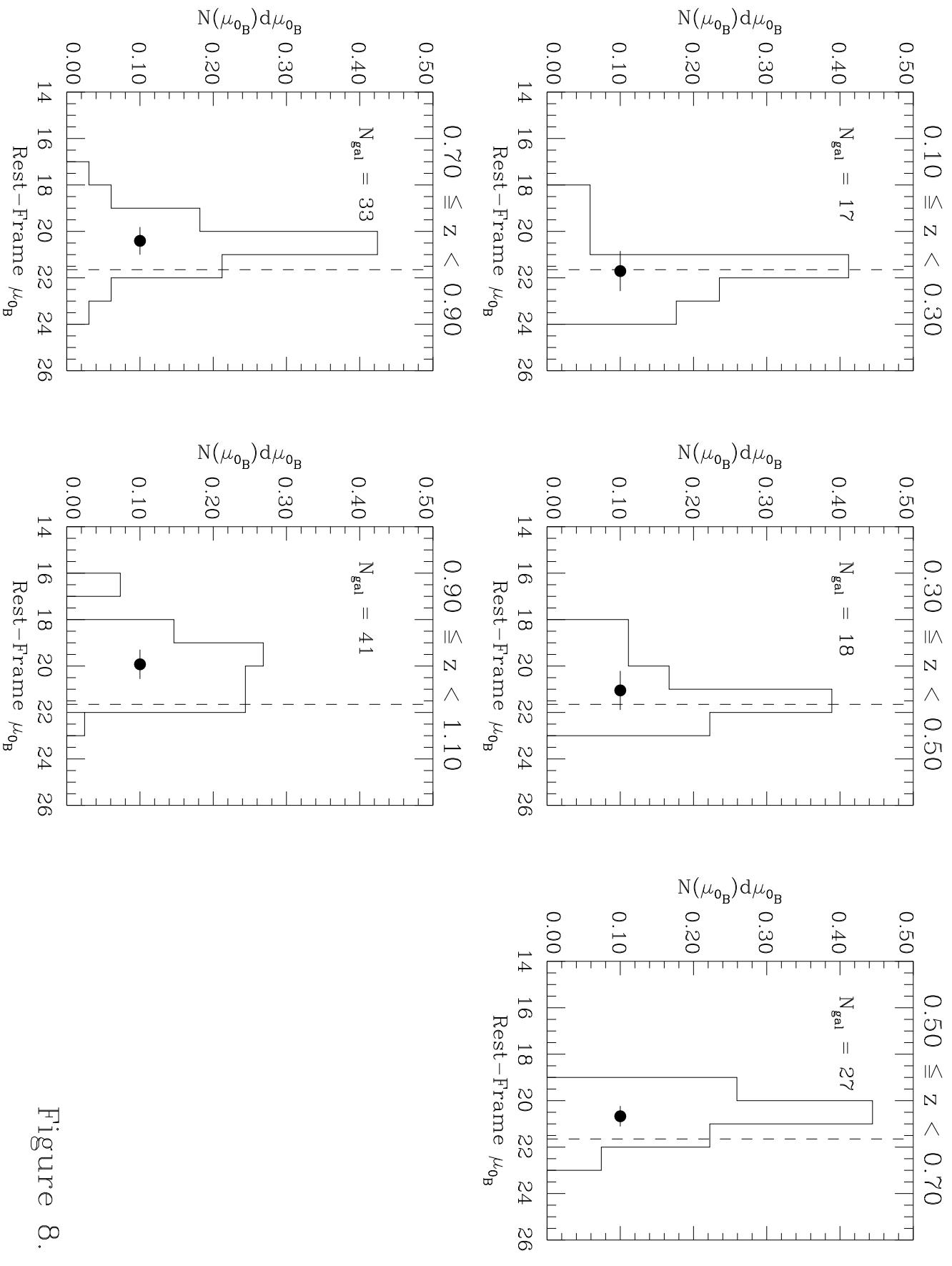


Figure 8.

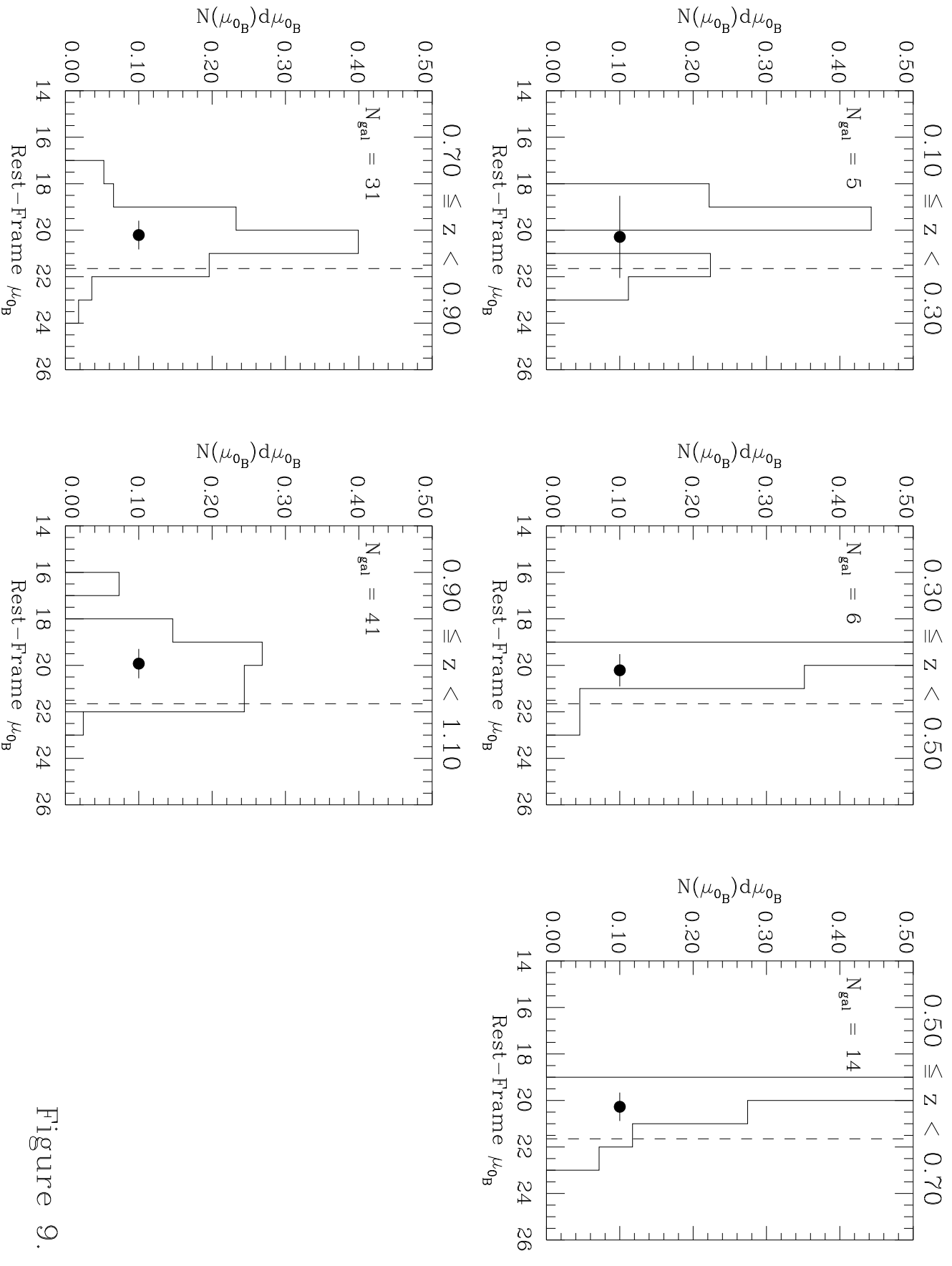
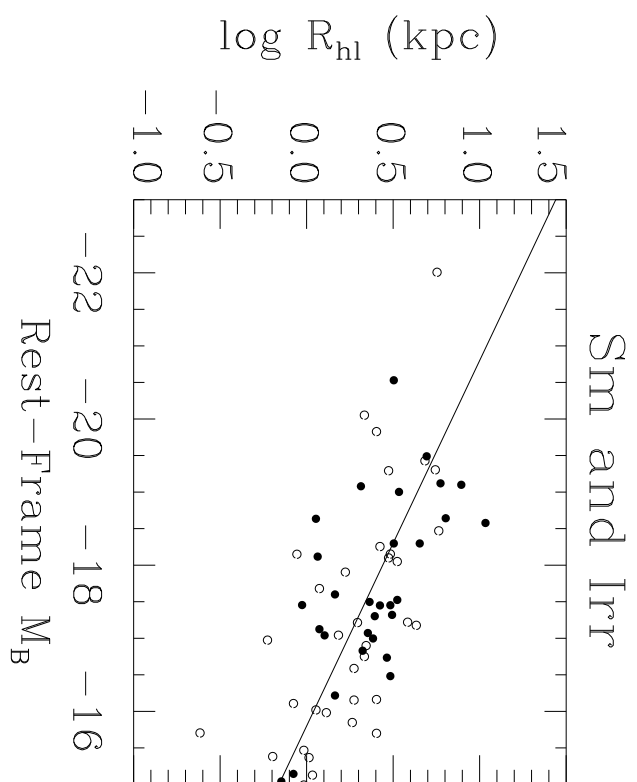
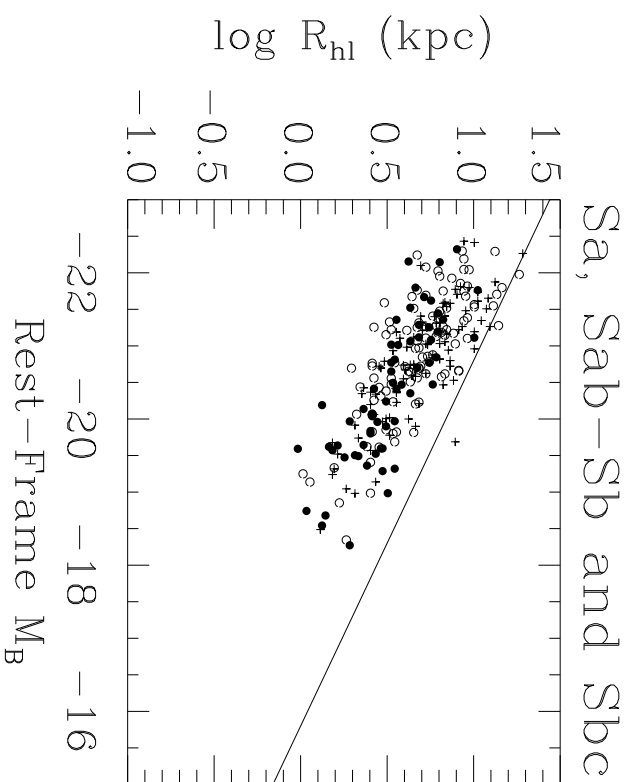
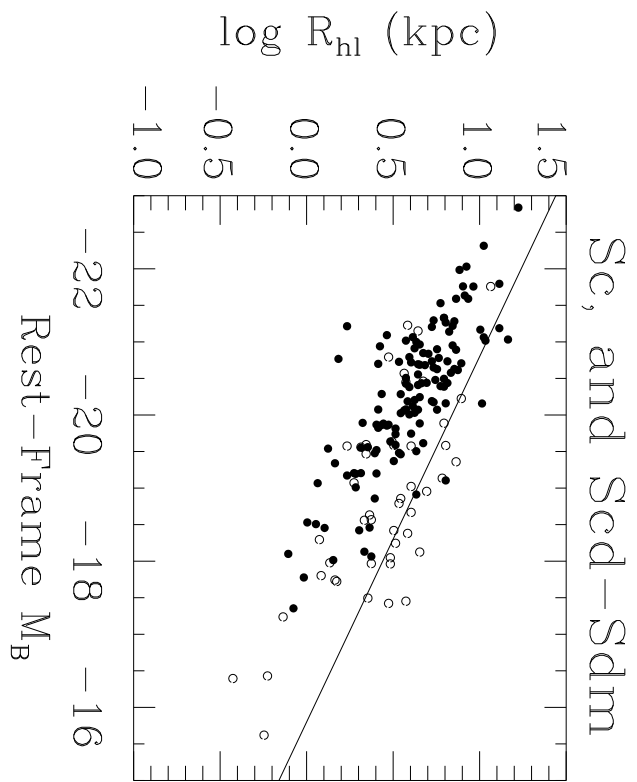
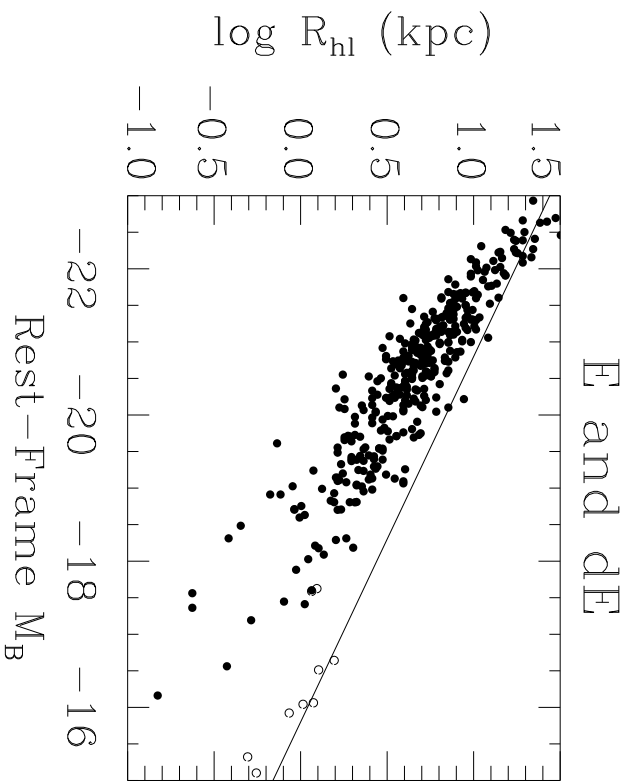


Figure 9.



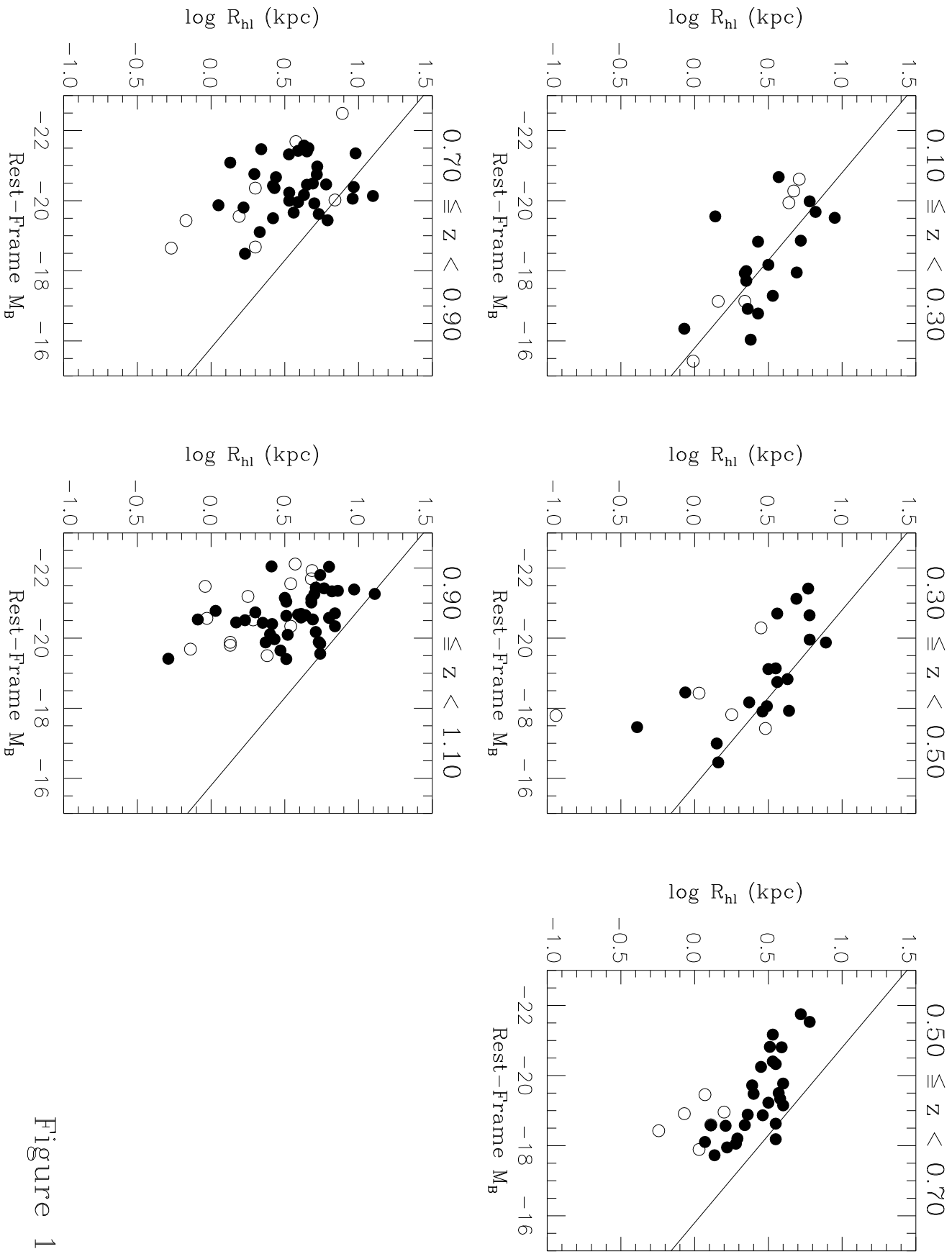


Figure 11.

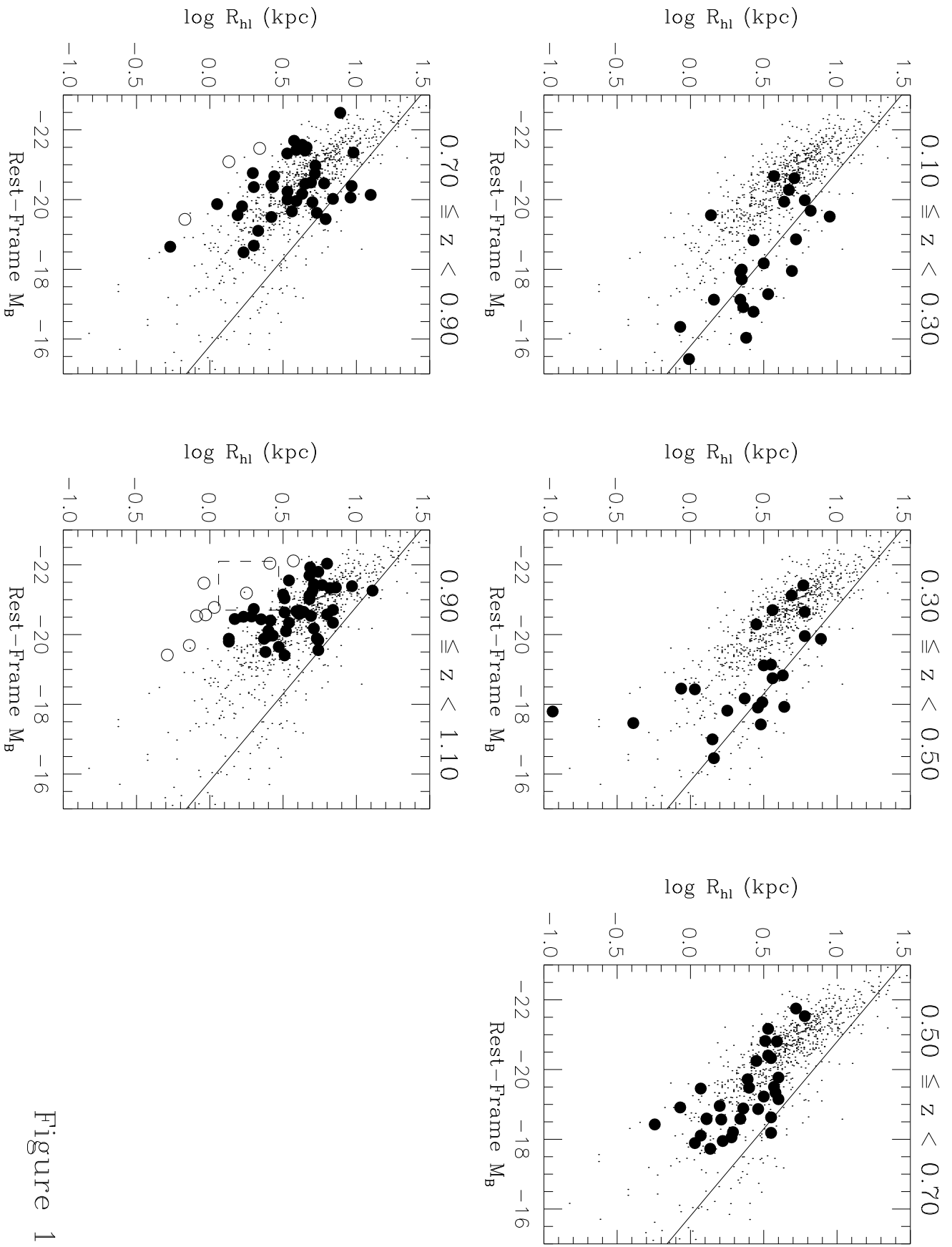


Figure 12.